This is a repository copy of *Pangea rifting and onward pre-Central Atlantic opening as the main ore-forming processes for the genesis of the Aouli REE-rich fluorite-barite vein system, Upper Moulouya District, Morocco*.

Article:

Accepted Manuscript

Pangean rifting and onward pre-Central Atlantic opening as the main ore-forming processes for the genesis of the Aouli REE-rich fluorite-barite vein system, Upper Moulouya District, Morocco

Daoud Margoum, Mohammed Bouabdellah, Andreas Klügel, David A. Banks, Francesca Castorina, Michel Cuney, Michel Jébrak, Gulcan Bozkaya

Please cite this article as: Margoum, D., Bouabdellah, M., Klügel, A., Banks, D.A., Castorina, F., Cuney, M., Jébrak, M., Bozkaya, G., Pangean rifting and onward pre-Central Atlantic opening as the main ore-forming processes for the genesis of the Aouli REE-rich fluorite-barite vein system, Upper Moulouya District, Morocco, *African Earth Sciences* (2015), doi: http://dx.doi.org/10.1016/j.jafrearsci.2015.03.021
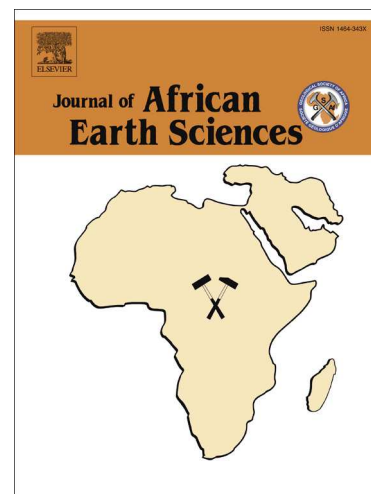
Pangean rifting and onward pre-Central Atlantic opening as the main ore-forming processes for the genesis of the Aouli REE-rich fluorite-barite vein system, Upper Moulouya District, Morocco

DAOUD MARGOUM & MOHAMMED BOUABDELLAH

Laboratoire des Gîtes Minéraux, Hydrogéologie & Environnement, Faculté des Sciences, 60000 Oujda, Morocco

ANDREAS KLÜGEL
Universität Bremen, Fachbereich Geowissenschaften, Postfach 33 04 40, 28334 Bremen, Germany

DAVID A. BANKS
School of Earth and Environment, University of Leeds, Leeds LS2 9JT, UK

FRANCESCA CASTORINA

Dipartimento di Scienze della Terra, Università ''La Sapienza'', P.le Aldo Moro, 00185 Rome, Italy
Istituto di Geologia Ambientale e Geoingegneria del CNR, Sezione di Roma ''La Sapienza'', Rome, Italy

MICHEL CUNEY
CREGU, GéoRessources, Université de Lorraine, CNRS, B.P. 239, 54506 Vandoeuvre lès Nancy, France

MICHEL JÉBRAK
Department of Earth and Atmospheric Sciences, UQAM, 201 President Kennedy boulevard, CP 8888 Centre Ville, Montreal, Québec, Canada H3C3P8

GULCAN BOZKAYA
Department of Geological Engineering, Pamukkale University, 20070 Denizli, Turkey

*Corresponding author: mbouabdellah2002@yahoo.f

Abstract

The Aouli fluorite-barite ± sulphides vein system in the Upper Moulouya District of Central Morocco is hosted in a folded and low to medium grade sedimentary and volcanic rocks, unconformably overlain by Permo-Triassic to Cretaceous red beds and limestones. Intrusion of the hydrothermally altered multiphase ca. ~330-319 Ma Aouli granite batholith has contact metamorphosed the host rocks to a metamorphic assemblage of cordierite, andalusite, chlorite, muscovite, and biotite ± sillimanite ± garnet.

The mineralized structures which consist mostly of quartz, fluorite, and barite occur principally as ENE-WSW, WNW-ESE, and E-W-trending trans-tensional steeply dipping veins, veinlets and en echelon tension gash fillings. Irrespective of color, location, paragenesis and textural position within the mineralized vein structure, the fluorite is characterized by high total REY contents ranging from 250 to 662 ppm, distinctive positive Eu and Y anomalies, and middle rare-earth element enrichment.

Fluid inclusion data indicate that the ore-forming fluids correspond to evolved NaCl-$CaCl_2$ + other cations sedimentary (94-174°C), saline (14-24 wt % NaCl equiv) brines. The strontium isotopic compositions of fluorite ($^{87}Sr/^{86}Sr$ = 0.710155-0.712293) and barite (0.710215-0.701401), along with the Liassic dolomitized limestones (0.707867-0.708140) are more radiogenic than the Cambro-Ordovician and Triassic-Early Jurassic seawater values, with the Aouli Late Variscan granite (0.70814±12) and the Triassic arkoses (0.709839-0.712313) displaying the highest $^{87}Sr/^{86}Sr$ ratios. Barite separates show uniform $\delta^{34}S$ ratios of +11 to +13.4‰ consistent with Permian-Triassic seawater sulphate.

The calculated REY fluid compositions along with fluid inclusion, strontium and sulphur isotope data point to the role of hot sedimentary brines with fluid-rock interaction at high fluid/rock ratios. The fluid system is likely related to the Pangea rifting and subsequent Central Atlantic opening during Permian-Triassic time. The fluorite-barite mineralization is likely due to mixing at the basement-cover interface of an ascending deep-seated fluid that equilibrated with Variscan crystalline basement rocks and cooler more dilute formation water.

1. Introduction

In North Africa as well as in Western and Central Europe, Variscan (Hercynian) orogenic belts and their unconformably overlying transgressive Mesozoic sedimentary rocks are host to some of the largest low temperature late- to post-Variscan fluorite-barite-base metal deposits (Sizaret et al., 2004; Munoz et al., 2005; Schwinn and Markl, 2005; Castorina et al., 2008; Piqué et al., 2008; Sanchez et al., 2009; Dill et al, 2011). Unlike European deposits whose mineralogy, fluid chemistry and age of emplacement are well established, North African deposits, and more specifically those of Morocco, remain poorly understood owing to the lack of geochronologic, fluid inclusion, and isotopic data.

In this respect, the Variscan Aouli inlier of the Upper Moulouya District and its unconformably overlying Mesozoic-Cenozoic cover (Fig. 1) are host to one of the largest Pb-Zn ± F ± Ba deposits of Morocco with a total production in excess of 31 Mt ore at ~4.5% Pb and <1 % Zn (Annich and Rahhali, 2002; Rahhali, 2002a, b). Beside Pb-Zn deposits, the Upper Moulouya District and particularly its lower Paleozoic stratigraphic section, contains dozens of uneconomic structurally-controlled F-Ba occurrences (i.e., the Aouli vein system described herein). Whereas the Pb-Zn mineralization was the focus of early exploration, the fluorite-barite occurrences have been neglected; being judged of too little economic interest. Prior to the present study, no detailed geochemical study had been undertaken on the fluorite-barite mineralization except for a few limited reconnaissance surveys (Jébrak, 1984 and unpublished mining reports). To fill such a gap, the present paper aims to: (1) characterize the rare earth element and Y (REY) compositions of the Aouli fluorite; (2) constrain the chemistry of the mineralizing fluids, (3) determine the fluid sources and related fluid-rock interactions; and (4) discuss the evolution of the mineralizing system and its implications for the understanding of ore-forming processes with respect to basin evolution and Variscan magmatism. The relationship between these fluorite-barite occurrences and the associated Pb-Zn mineralization is beyond the scope of the present paper.

2. Geologic Setting

2.1. Stratigraphy

The Upper Moulouya District stratigraphy consists of a succession of greenschist to amphibolite Lower Paleozoic sedimentary, volcaniclastic and volcanic rocks, and an unconformably overlying Mesozoic and Cenozoic package (Emberger, 1965; Fig. 1). The Lower Paleozoic sequence, locally intruded by the hydrothermally altered multiphase Aouli

109 granite batholith, consists of an up to 3,800m thick succession of Cambro-Ordovician
110 metasediments mainly metapelites, metaquartzites, metagraywackes, and minor metatuffs
111 with interbedded mafic amphibolites. This metasedimentary package has been interpreted as
112 representing turbiditic sequences deposited in a tectonically active continental margin setting
113 (Vauchez, 1976; Filali, 1996; Filali et al., 1999), whereas the emplacement of the interbedded
114 amphibolites was related to the Early Cambrian extension (Ouali et al., 2000).

115   Regional metamorphic grades range from greenschist to amphibolite facies.
116 Conversely, thermal metamorphism produced by the emplacement of the Aouli batholith
117 gave rise to a regionally developed metamorphic aureole that consists predominantly of
118 spotted-textured schists with porphyroblasts of cordierite, andalusite, chlorite, muscovite, and
119 biotite ± sillimanite ± garnet (Filali, 1996, Dahire, 2004). These metamorphic mineral
120 assemblages indicate peak thermal conditions ranging from 400 to 550°C and pressures less
121 than 3 kb, corresponding to batholith emplacement depths ranging from 4 to 7 km (Filali,
122 1996, Dahire, 2004).

123   Unconformably overlying the Paleozoic package is a ~400-500m sequence of red-bed
124 Permian-Triassic sediments consisting of basal conglomerates, sandstones, arkoses, with
125 gypsum and salt-bearing argillites interbedded with tholeiitic basalt sills, followed by up to
126 1,000 metres of tabular Jurassic and Cretaceous shallow marine carbonates and marls locally
127 intruded by alkaline basaltic lava flows dated at 14.6 to 0.5 Ma (Harmand and Cantagrel,
128 1984; Duggen et al., 2009; Wittig et al., 2010). Paleogeographically, the Upper Moulouya
129 District acted as an uplifted basement high that was eroded during the end of the Variscan
130 orogeny and the beginning of Permian time (Ouarhache et al., 2012).

131   The tectonic structures resulting from both the Variscan and Atlasic orogenies are
132 dominated by a succession of tight to isoclinal folds with fracture cleavage or flow
133 schistosity, along with a series of dominant E-W-trending and sub-ordinate ENE-WSW, NW-
134 SE and WNW-ESE multiple kilometre-scale faults.

135

136 *2.2. Aouli batholith and chronology*
137 The Aouli intrusive complex occurs as an elongate ENE-trending 15 km x 25 km, multiphase,
138 oval-shaped, sub-concentric zoned batholith covering a total area of ~ 260 km^2 (Fig.1). The
139 petrography and geochemistry of the Aouli batholith have been well described through
140 multiple investigations (Emberger, 1965; Clauer et al., 1980; Tisserant, 1977; Diot and
141 Bouchez, 1989; Rosé, 1987; Oukemeni, 1993; Oukemeni and Bourne, 1994; Oukemeni et al.,

142 1995; Dahire, 2004). Only a summary of the main conclusions which are relevant to the
143 present study are given below.

144   Based on geochemistry, age dating isotopic data, and crosscutting relationships, the
145 Aouli intrusive complex is subdivided into three major mapable plutonic associations (Fig.
146 1): (1) El Hassir apophysis, (2) Aouli-Bou Mia (Aolui *ss*), and (3) Poulet-Perdreaux
147 intrusions. These intrusions are texturally, mineralogically, and geochemically different.
148 They range from porphyritic through fine- to coarse-grained, and show a compositional
149 spectrum from monzodiorite to leucogranite. The El Hassir apophysis, dated at 347-328 Ma
150 (Clauer et al., 1980; Oukemeni, 1993; Oukemeni and Bourne, 1994; Oukemeni et al., 1995;
151 Dahire, 2004), was emplaced before the 329-319 Ma Aouli *ss* intrusion (Tisserant, 1977;
152 Clauer et al., 1980; Oukemini, 1993; Oukemeni and Bourne, 1994; Oukemeni et al., 1995)
153 which in turn preceded the 308-281 Ma Poulet-Perdreaux leucogranite (Tisserant, 1977;
154 Clauer et al., 1980). The Rb-Sr age of ca. 281 Ma should be, however, taken with care as the
155 Rb-Sr dating method is known to decrease the reliability of the calculated radiometric ages
156 depending on the alteration state of the analyzed samples (i.e., rejuvenation phenomenon). By
157 discarding conflicting radiometric ages, we therefore confidently conclude that the
158 emplacement of the multiphase Aouli pluton occurred in middle to late Carboniferous time
159 ca. ~330-319 Ma.

160   Pervasive hydrothermal alteration affected, to varying degrees, the Aouli batholith
161 resulting in the development of microcline, albite, chlorite, episyenites, and greisenization of
162 all the granitic units**.**

163 **3. Fluorite-barite mineralization: mode of occurrence, mineralogy, textures and**
164 **paragenesis**

165 Based on the stratigraphic position, the geometry of the ore occurrences, and the process of
166 ore formation, two distinct types of epigenetic fluorite-barite mineralization are distinguished:
167 (i) structurally controlled open-space filling, and to a lesser extent (ii) metasomatic
168 replacement.

169   *Open-space filling* mineralization which is by far the dominant mineralization style
170 consists of a complex system of mineralized trans-tensional sub-vertical veins (Fig. 2A),
171 veinlets and en echelon tension gash fillings. The veins occur both within the Aouli granitic
172 intrusion and the schistose Cambro-Ordovician country rocks close to the basement-cover
173 unconformity. In this respect, four fluorite-barite ± sulphides vein systems, referred to as Sidi
174 Ayad, Aouli, Sidi Said, and Ansegmir are recognized (Fig. 1). The veins of the Ansegmir

175 system occur in the fracture zones within the granitic intrusion, those of Aouli and Sidi Said

176 systems are enclosed within the Cambro-Ordovician schists, whereas the mineralized veins of

177 Sidi Ayad occur along strike within granitic and schistose host rocks.

178   The veins are up to 4 m wide and 400 m long, spaced 50 to 100 m apart, strike ENE-

179 WSW, WNW-ESE, and E-W (Fig. 1), and are steeply dipping (70° to ~90°). Locally, some

180 mineralized veins occur as conjugate vein pairs and en echelon tension gash. Texturally, the

181 veins display comb (Fig. 2B), cockade, laminated, breccia and crack and seal textures,

182 suggesting that episodic, multiple mechanisms were important for trans-tensional vein

183 formation. Small vug-filling disseminations of yellow fluorite and barite ± sulphides also

184 occur within the Triassic red arkoses (Fig. 2C) in agreement with the observations of

185 Dagallier (1983) and Jébrak (1984). Replacement mineralization, which is of little economic

186 interest, occurs as disseminations or clusters of barite and fluorite crystals of variable-grain

187 size replacing pre-existing sedimentary structures.

188   Overall, the Aouli fluorite is massive and yellowish-colored throughout, though locally

189 may have oscillatory zoning (Fig. 2D) and well-developed cubic fluorite crystals lining vugs

190 are present (Fig. 2E). Greenish, colorless and purple fluorite varieties are also locally present.

191 Sulphides are locally abundant and consist of variable amounts of galena, sphalerite, pyrite, and

192 chalcopyrite. Barite occurs either as massive aggregates or crested white to pink crystals

193 encrusting voids. Carbonates are virtually absent but quartz is abundant.

194   The sequence of mineral deposition shows the existence of two successive stages of

195 mineralization, (i.e., stages I and II) which are of economic interest (Fig. 3). These two stages

196 are distinguished by megascopic and microscopic textural and cross cutting relationships

197 although both stages display the same mineral assemblages. Stage I, referred to as "main-ore

198 stage", is the earliest and economically the most important, accounting for more than 90

199 percent of the total fluorite-barite resources. The mineral paragenesis consists of fluorite (F-1)

200 in addition to quartz (Qz-1) and barite (Ba-1) (Fig. 3).

201   Conversely, stage II mineralization consists of variably colored, cm-sized cubic fluorite

202 (F-2), crested white to pink barite (Ba-2), and drusy quartz (Qz-2) crystals lining vugs. This

203 stage is referred to as "late-ore cuboctahedral stage".

204 The post-ore supergene mineral assemblage (stage III) resulting from the oxidation of

205 primary sulphides consists of minor amounts of cerussite, malachite, azurite and Fe and Mn

206 oxides.

207

208

4. Age of mineralization

No radiometric age is available yet for the Aouli fluorite-barite ± sulphides mineralization. Thus, combined geological field observations and textural cross-cutting relationships were used to bracket the relative timing of mineralization.

In this respect, the fluorite-barite ± sulphides mineralization is structurally controlled, and the mineralized vein structures crosscut both the dominant regional S_{2-3} foliation and the Late Variscan (middle to late Carboniferous) ca. 330-319 Ma Aouli granitic intrusion. Moreover, the fluorite-barite ± sulphides mineralization extends to well above the Paleozoic basement into the unconformably overlying Triassic basal arkoses as fluorite and barite disseminations or clusters of varying grain size (Dagallier, 1983; Jébrak, 1984; and the present study). However, the overlying Liassic carbonate strata are devoid of any trace of fluorite mineralization. Together, these relationships indicate that the fluorite-barite ± sulphides mineralization occurred late in the tectonic history of the Aouli area, toward the end of the latest phase of Variscan ductile deformation (i.e., during the Permian-Triassic times; Hoepffner et al., 2006) and before the Liassic. Thus, the inferred age of the Aouli fluorite-barite ± sulphides mineralization is constrained as being between Permian and Triassic time.

Recently, Cheilletz et al. (2010) proposed, for the nearby El Hammam fluorite vein-type deposit (Fig. 1), whose geological context and fluorite mineralogy and geochemistry (i.e., REE contents) are very similar to those of the studied Aouli vein system, a $^{40}Ar/^{39}Ar$ age of 205 ± 1 Ma. However, it should be stressed that this radiometric age was recorded on paragenetically later adularia crystals rather than on fluorite itself, constraining therefore the Triassic as a minimum age of mineralization. Based on these geological and geochronological constraints, we can confidently conclude that the Aouli fluorite-barite ± sulphides mineralization occurred sometime between Permian and Triassic time coincident with the early stages of Pangea rifting and subsequent Central Atlantic opening (Irving, 1977; Klitgord and Schouten, 1986; Piqué and Laville, 1993; Ricou, 1994; Torcq et al., 1997; Muttoni et al., 2003, Martins et al., 2008). This inferred time span coincides with $^{40}Ar/^{39}Ar$ radiometric ages (220-155 Ma; Valenza et al., 2000) and recent apatite fission track thermal modeling data which indicate hydrothermal event ages between 250 and 210 Ma (Ghorbal et al., 2008; Saddiqi et al., 2009; Barbero et al., 2011).

243 **5. Sampling and analytical procedures**

244 *5.1. Sample strategy*

245 Fluorite and barite separates of different habits and colors deposited through the main

246 paragenetic stages (Fig. 3) were collected from the Aouli vein surface outcrops, and

247 abandoned mine galleries. The selected mineral separates were handpicked under a binocular

248 microscope to ensure the samples were clean and pure. Visibly fresh host rocks, from field

249 exposure expected to constitute potential source rocks for the fluorite-barite ± sulphides

250 mineralization, were also selected for bulk-rock geochemical analysis. Petrographic studies

251 were carried out by visual examination of hand specimen material complemented by

252 transmitted and reflected light microscopy of polished thin sections.

253 *5.2.Whole-rock geochemistry*

254 Granite, arkose, and dolostone powders were analysed by ICP-AES for major elements and

255 ICP-MS for 43 trace elements at the SARM laboratory (CRPG and CNRS, Nancy, France)

256 using the Carignan et al. (2001) methodology and standards.

257

258 *5.3. Laser ablation-ICP-MS*

259 Trace element contents of fluorite were determined by laser-ablation inductively coupled

260 plasma-mass spectrometry (LA-ICP-MS) at the Institute of Geosciences, University of

261 Bremen, using a NewWave UP193 solid-state laser coupled to a ThermoFinnigan

262 Element2™. Samples on thin sections and standards were ablated as line scans at 5-10 $\mu m \cdot s^{-1}$

263 with spot sizes of 75 µm and a laser pulse rate of 5 Hz. Plasma power was 1200 W, Helium

264 (0.4 $l \cdot min^{-1}$) was used as sample gas, and Argon (0.8 $l \cdot min^{-1}$) was subsequently added as

265 make-up gas. All isotopes were analysed at low resolution with five samples in a 20% mass

266 window and a total dwell time of 25 ms per isotope. Blanks were measured for 20 s prior to

267 ablation. After every 5-10 samples NIST612 glass was analysed as an external calibration

268 standard using the values of Pearce et al. (1997). For data quantification the Cetac GeoPro™

269 software was used with ^{43}Ca as internal standard, assuming ideal stochiometric compositions

270 of fluorite. Data quality was assessed by analyses of USGS glass reference materials BCR2G

271 and BHVO2G along with the samples (Table 1). External precision over three days of

272 analyses is <10 % for most elements; this value includes heterogeneities of the standard

273 materials used and is typically <5 % if consecutive analyses within small areas are carried

274 out. Accuracy as determined by comparison with the GeoReM data base (picked by January

275 2009) is <10 % for most elements.

5.4. Fluid inclusion analysis

Microthermometric measurements of fluid inclusions in fluorite were performed at Universitat Autonoma of Barcelona (Spain) on 20 doubly polished sections using a Linkam heating-freezing stage and a Fluid Inc. USGS-adapted gas-flow heating and cooling stage that had been calibrated at -56.6°, 0.0°, and 374.1°C using Syn Flinc standards. Uncertainty in the microthermometric measurements was ±0.1°C between -100 and 25°C and increased linearly to ± 3.0°C between 100° and 250°C and between -100° and -196°C. For the Fluid Inc. stage, uncertainties were ±1 to 5°C for temperatures between 100 and 250°C, ±0.2°C between -40 and 100°C, and ±0.5°C between -40 and -150°C.

It should be stressed that the fluid inclusions were not studied within the framework of Fluid Inclusion Assemblages (FIAs) sensu stricto (Goldstein and Reynolds, 1994). Rather, fluid inclusions were grouped according to the stage of mineralization and host phase. This approach is similar to that developed by Preece and Beane (1982) to associate fluid inclusions with specific alteration/mineralization events when FIAs cannot be discriminated.

5.5. Strontium isotope analysis

The Sr isotope analyses were carried out at the Institute of Environmental Geology and Geoengineering (IGAG-CNR), University of Rome "La Sapienza" according to the procedure described in Castorina et al. (2008) using a FINNIGAN MAT 262RPQ multi-collector mass spectrometer in static mode. Strontium was run on Re double filaments. The internal precision (within-run precision) of a single analytical result is given as two-standard errors of the mean. Repeat analyses of standards gave averages and errors expressed as two-standard deviations (2σ) as follows: NBS 987 $^{87}Sr/^{86}Sr$ = 0.710255±0.000030 (n = 16), $^{86}Sr/^{88}Sr$ normalized to 0.1194. Total procedural blanks were below 2 ng Sr.

5.6. Sulphur isotope analysis

Barite extractions and analyses were carried out at the Environmental Isotope facilities of the University of Waterloo (Canada) using an Isochrom Continuous Flow Stable Isotope Ratio Mass Spectrometer GVI Micromass coupled to a Carlo Erba Elemental Analyzer CHNS-O EA1108. The followed experimental procedure involved the liberation of SO_2 gas by rapid combustion of the samples with vanadium pentoxide. The data are reported as per mil (‰) deviations relative to the Canyon Diabolo troilite (CDT) standard. The analytical uncertainty (2σ) was ±0.12 ‰.

6. Result*s*

6.1. *REE and trace element compositions of fluorite*

Fluorite separates from the Sidi Said, Sidi Ayad, Ansegmir and Aouli vein systems show roughly similar trace elements concentrations irrespective of their color, location, paragenesis or textural position within the vein structure (Table 1). In addition to REE and Y (REYs), high field strength elements such as Nb, Ta, U, Th, Zr, and Hf are present in very small concentrations, commonly close to the detection limit. Sr and Rb concentrations range from 49 to 381 ppm, and 0.1 to 0.5 ppm, respectively. These abundance ranges are significantly lower than those recorded for the host rocks (i.e., dolostone, granite and arkose; Table 1).

Overall, the Aouli fluorite is characterized by high total REY concentrations (ΣREY) ranging from 250 to 662 ppm (Table 1). Although there is no significant difference in normalized REY patterns for fluorite from the different vein systems (Fig. 4), fluorite from the Ansegmir system tends to exhibit the highest ΣREY concentrations (average = 648 ppm; n = 9) whereas fluorite from Aouli system displays the lowest ΣREY contents (average = 187 ppm; n = 2). Fluorite separates from the Sidi Ayad and Sidi Said vein systems have closely similar intermediate ΣREY concentrations (Fig. 4). The fluorite separates from the four vein systems display similar PAAS-normalized "hump"-shaped REY patterns that are depleted in light (LREE) and heavy (HREE) rare earth elements but significantly enriched in middle rare earth elements (MREE), in addition to exhibiting positive Y and Eu anomalies with Eu/Eu* ratios of 1.4 to 4.5, but lack of a Ce anomaly (Fig. 4). In the discriminative Tb/La versus Tb/Ca diagram of Möller et al. (1976), all of the analyzed fluorite samples plot within the pegmatitic field (Fig. 5).

Compared to fluorite veins, whole-rock compositions of the Aouli granite and the overlying Triassic arkose and Liassic carbonate host rocks show substantially lower ΣREY concentrations (Table 1). The PAAS-normalized REE pattern of the Aouli granite (Fig. 4) displays a weak global fractionation with a roughly flat shape, coupled with a large negative Eu anomaly, typical of A-type highly fractionated, high-K, calc-alkaline granites (Taylor, 1982; Pérez-Soba and Villaseca, 2010). However, the Liassic carbonate shows the lowest ΣREY concentrations of 17 ppm, and a roughly flat PAAS-normalized REE pattern (Fig. 4). Although the relative enrichment or depletion of individual elements varies for fluorite separates from the different vein systems, the shapes of the REY patterns are broadly similar (Fig. 6), indicating a common origin for all the analyzed fluorites.

343 *6.2. Sulphur isotope compositions*

344 A representative suite of ten barite samples were analyzed for their sulphur isotope

345 compositions. Of these, seven samples are from the Paleozoic-hosted main vein systems and

346 the remaining three samples are from the unconformably overlying Triassic arkoses. Only

347 samples containing coexisting fluorite and barite crystals were analyzed (Table 2). Karst

348 filling barite from the overlying Liassic dolomitized limestones (i.e., Mibladen deposit, Figs.

349 1, 2), commonly associated with sulphide-rich mineralization of Mississippi Valley affiliation

350 (Naji, 2004) and correlatively free of fluorite, was not included in the course of the present

351 study as it is interpreted (Jébrak et al., 1998) as resulting from a separate later hydrothermal

352 system unrelated to the fluorite-barite mineralizing event described herein.

353 Except for sample 11-ALB$_3$ (Table 2) which shows the lightest δ^{34}S value of 8.6‰, all

354 the analyzed barite samples have a rather uniform range of δ^{34}S ratios from +11 to +13.4‰

355 (avg = +12.2‰, σ = 1.4‰, n = 9), consistent with values for sulphates precipitated from

356 Permian to Triassic seawater (i.e., +11 to +18‰; Claypool et al., 1980; Strauss, 1997) (Fig.

357 7). Moreover, the distribution of δ^{34}S ratios displays neither spatial (lateral and vertical) nor

358 temporal compositional variations. These data compare to δ^{34}S values of +8.9 to +14.7‰ for

359 vein and karst barite deposits of Western Jebilet reported by Valenza et al. (2000), but

360 contrast significantly with those values documented for the Bouznika Cambrian barite deposit

361 (δ^{34}S = +31-38‰; Jébrak et al., 2011).

362

363 *6.3. Strontium abundances and Sr isotope compositions*

364 Strontium isotope compositions were determined for six whole-rock samples that include the

365 dominant country rocks (i.e., three Liassic dolomitized limestones, two Triassic arkoses and

366 one Late Variscan granite), and for 22 mineral separates of which 16 fluorite and six barite

367 span the sequence of mineral deposition (Fig. 3). The results are summarized in Table 3 and

368 shown in Figure 8. Low Rb/Sr in dolomite, fluorite and barite imply that the present-day

369 ^{87}Sr/^{86}Sr values have not been affected by *in situ* decay. Conversely, strontium isotope

370 compositions for the Late Variscan granite and the Triassic arkosic samples have been

371 corrected for decay of ^{87}Rb since the time of ore deposition interpreted to have occurred, as

372 discussed above, at 250 Ma (Permian-Triassic).

373 The fluorite separates are characterized by a wide range of Sr concentrations from 49 to

374 381 ppm, whereas barite tends to have higher Sr contents (148-308 ppm) (Table 3). The

375 Liassic dolostones exhibit the highest Sr concentration of 3429 ppm (Table 3). These

376 variations in Sr concentrations are roughly correlated with variable $^{87}Sr/^{86}Sr$ ratios (Fig. 9).

377 There is, however, no correlation between the colour of fluorite and its Sr isotopic

378 composition.

379 Nevertheless, the $^{87}Sr/^{86}Sr$ ratios of fluorite and barite overlap partially or wholly with

380 those reported for Liassic dolomitized limestones and Triassic arkoses (Fig. 9). Indeed, the

381 $^{87}Sr/^{86}Sr$ ratios of the barite range from 0.708173 to 0.711401 (avg 0.709715, n = 7); with

382 barite samples from the Cambro-Ordovician schists being more radiogenic (0.701401-

383 0.710215) than those from the overlying Triassic arkoses and Liassic dolomitized limestones

384 (0.708173-0.708500) (Table 3; Fig. 8). Similarly, the $^{87}Sr/^{86}Sr$ ratios of the fluorite vary in a

385 wide range (0.710155-0.712293) from one vein system to another, and even within the same

386 vein system with the highest ratios corresponding to fluorite separates from Ansegmir

387 (0.711701-0.711893), and Aouli (0.710923-0.712293) vein systems (Table 3; Fig. 8).

388 Overall, most of the measured $^{87}Sr/^{86}Sr$ ratios are more radiogenic than the Cambro-

389 Ordovician and Triassic-Early Jurassic seawater values of 0.7075 to 0.7070 (Burke et al.,

390 1982; McArthur et al. 2001) (Fig. 9). Nevertheless, the $^{87}Sr/^{86}Sr$ ratios of Liassic dolomitized

391 limestones (0.707867-0.708140) are close to those reported for barite hosted by the Triassic

392 arkoses (Table 3). Conversely, the Late Variscan granite displays the highest $^{87}Sr/^{86}Sr$ ratios

393 of 0.718510±21.

394

395 *6.4. Fluid inclusion studies*

396 *6.4.1. Petrography*

397 Fluid inclusions were studied in different color and textural varieties of fluorite from the four

398 main vein systems encompassing the Aouli district. Fluid inclusions in barite, though initially

399 investigated, were ultimately omitted due to the known strong susceptibly of barite to stretch

400 or leak during heating (Ulrich and Bodnar, 1988). We note, however, that fluid inclusions in

401 fluorite may also stretch if the internal pressure exceeds a few hundred bars (Bodnar, 2003).

402 Large fluid inclusions tend to stretch at lower internal pressures compared to smaller

403 inclusions (Bodnar, 2003), and some of the inclusions in this study are unusually large (>100

404 µm) (Fig. 10).

405 The fluid inclusions are classified as primary (P), pseudosecondary (PS), or secondary

406 (S) according to the criteria of Roedder (1984). Most of the investigated fluid inclusions,

407 which range in size from 60 to less than 10 µm, occur either as trails of regular to irregularly-

408 shaped inclusions (i.e., oval, rounded or elongated) distributed along secondary fractures and

409 cracks that crosscut the primary growth zones (i.e., PS and S fluid inclusions), or more rarely

410 along growth zones (P), or as scattered and isolated fluid inclusions exhibiting consistently
411 regular cubic, tabular, elongated or wedge-shaped negative-crystal forms (Fig. 10). These
412 latter forms are considered to be primary fluid inclusions, although we recognize that this
413 criterion is not always diagnostic.

414 Based on the number of observable phases present at room temperature, all inclusions
415 are two-phase (liquid and vapor) that contain approximately 85 vol percent liquid, with
416 relatively uniform vapor/liquid ratios. In a few samples, some liquid only inclusions were
417 observed, but these are relatively rare. No clathrates or visual evidence of CO_2 was detected
418 at room temperature or on cooling, however very occasionally some inclusions contained
419 birefringent solids (Fig. 10D). As these are scarce and that other inclusions associated with
420 these do not contain solids we suggest these are accidentally trapped and not daughter
421 crystals.

422

423 *6.4.2. Thermometric and salinity measurements*
424 Microthermometric measurements were performed exclusively on liquid-vapour inclusions
425 that homogenized by disappearance of the vapor bubble. In this respect, temperatures of first
426 (T_e) and final ice ($T_{m(ice)}$) melting along with final melting of hydrohalite ($T_{m(hh)}$), and vapor-
427 liquid homogenization temperature (T_h) were determined for 275 inclusions with the
428 temperature of final ice and hydrohalite melting measured for 188 and 103 of these
429 inclusions; respectively. Data are reported in Table 4 and plotted in Figures 11 and 12. Fluid
430 salinities were calculated using the HOKIEFLINCS_H_2O-NaCl software of Steele-MacInnis
431 et al. (2012).

432 Initial ice-melting temperatures ranging from -44° to -93°C (Table 4), well below the
433 eutectic of the pure NaCl-H_2O and NaCl-KCl-H_2O systems (Crawford, 1981), are consistent
434 with Ca+K+Na+Mg brine ($T_{e(MgCl2)}$ = -35°C, Dubois and Marignac, 1997; $T_{e(CaCl2)}$ = -52°C,
435 Davis et al., 1990). Eutectic melting at -93°C is unrealistic and it is more likely to be
436 recrystallization of the ice-glass which is often observed. In the alkali and alkaline earth
437 chloride system lower T_e values of ~-65°C are possible due to a metastable eutectic. The
438 distribution of salinities of P and PS inclusions (expressed as wt% equivalent NaCl) and
439 homogenization temperatures for the four vein systems are shown in Figures 11 and 12.
440 There was no distinction in salinity or homogenization temperature based on the inclusions
441 being classified as P or PS. Overall there is a wide spread of the final ice melting
442 temperatures, $T_{m(ice)}$ range from -20° to -6°C, reflecting fluid salinities that vary from 24 to 13
443 wt% equiv. NaCl. Individually the vein systems have salinities that are more tightly

444   constrained indicative of a single fluid at each vein system but with marked variability

445   between deposits (Fig. 12). Hydrohalite dissolved at temperatures ranging from -25.5 to -

446   18.6 (Table 4). In some inclusions the temperature of hydrohalite and ice coexistence is

447   above the eutectic temperature of the H_2O-NaCl system which is not possible unless there is

448   an additional anion present in the fluid. However, the temperatures are only slightly higher

449   and we suggest this is due to the slow melting of hydrohalite as the temperature was

450   increased and that these inclusions are dominated by NaCl with less $CaCl_2$ than other

451   measured inclusions. The $T_{m(ice)}$ and $T_{m(hh)}$ pairs for the different vein systems are shown in

452   Figure 13 where fluid inclusions from Ansegmir have the greatest $CaCl_2$ concentration and

453   samples from other veins are primarily NaCl fluids. Inclusions from Aouli and the majority

454   from Sidi Ayad have $T_{m(hh)}$ at temperatures above the T_e for NaCl-H_2O fluids (discussed

455   above) and would plot on or very close to the H_2O-NaCl axis of the ternary diagram. Fluid

456   inclusions in fluorite from the Ansegmir vein system have the highest salinities (22-24 wt %

457   NaCl equiv), whereas those from the Sidi Said and Aouli vein systems exhibit the lowest

458   salinities with an average value of ~16 wt % NaCl equiv. Intermediate salinities of ~20 wt %

459   NaCl equiv are recorded in fluorite from the Sidi Ayad vein system (Fig. 12).

460   The homogenization temperatures of the inclusions from the different vein systems

461   cover a large range from ~90 to ~180°C, but in individual veins the minimum variation is~

462   40°C (Fig. 11). Inclusions from the Aouli and Sidi Ayad veins have average T_h values of

463   119°C and 110°C respectively, that are statistically the same at a 95% confidence limit.

464   Similarly inclusions from the Sidi Said and Ansegmir veins have average T_h values of 139°C

465   and 147°C respectively that are statistically the same at a 95% confidence limit, but are also

466   statistically different to those of the other 2 vein systems at the same confidence level.

467   Therefore we interpret there to be 2 distinct fluid temperatures in these localities. The

468   variability of the T_h values at individual vein system is outwith what would be expected from

469   measurement uncertainties (perhaps with the exception of inclusions from Aouli) and may be

470   due to either stretching of the inclusions due to overheating or fluctuations in pressure during

471   mineral deposition. Stretching or leaking of soft minerals, such as fluorite and barite, can

472   occur during microthermometry (Bodnar and Bethke 1984, Ulrich and Bodnar 1988) with the

473   amount of stretching related to the increase in the internal pressure which depends on the size

474   of the inclusions and the amount of overheating. However, for fluorite hosted inclusions the

475   amount of overheating required to vary the T_h values by the amounts recorded would not be

476   achieved during microthermometry. The alternative of variations in pressure from greater

477   than hydrostatic, perhaps initially close to lithostatic, and then lowering to hydrostatic as the

478 hydrothermal system developed is more plausible. This would cool the fluids due to adiabatic

479 expansion to the degree recorded in the inclusions. Most of the fluid inclusion temperatures

480 are at the lower end of the recorded range and this is consistent with the pressure being

481 hydrostatic and with fluid flow and mineral deposition being at a maximum**.**

482

7. Discussion

484 *7.1. REE constraints on fluid source(s)*

485 The high REE contents of the Aouli fluorite (up to 720 ppm; Table 1) impose specific

486 requirements in term of fluid source(s) and fluid-rock interactions. Unlike low REE-bearing

487 fluorite deposits whose genesis have been shown to be related to sedimentary basinal

488 hydrothermal brines, the origin of high REE-bearing fluorite deposits remains controversial

489 (Cheilletz et al., 2010). Classically, REE enrichment has been shown to occur during

490 magmatic evolution in alkaline-carbonatite or A-type granite intrusive environments

491 (Schönenberger et al., 2008; Cheilletz et al., 2010; Bouabdellah et al., 2010). The discrepancy

492 between the PAAS-normalized REY patterns of the Aouli fluorite and the adjacent granitic

493 intrusion (Fig. 5) constitutes evidence for the disconnection between the fluorite-barite

494 mineralization and felsic magmatism. In support of this statement, the trivalent REE patterns

495 of the parent fluid which precipitated the Aouli fluorite, calculated using a lattice-strain

496 model with parameters from van Hinsberg et al. (2010), closely mimic those of the

497 precipitating fluorite (Fig. 14). The resulting calculated fluid strongly differs from that of a

498 magmatic fluid exsolved from a crystallizing granite melt, as it would have had very low

499 REY concentrations (about 10^{-6} to 10^{-5} PAAS-normalized) coupled with a pronounced LREE

500 depletion; and $(Eu/Eu^*)_{PAAS}$ ratios in the range of ~0.1 to 4 depending on the oxygen

501 fugacity.

502 Based on these thermodynamic constraints, we propose that the high REE contents of

503 the Aouli fluorite is inconsistent with the involvement of purely magmatic fluids, pointing

504 instead to the role of hot basin-derived brines and subsequent fluid-rock interaction at high

505 fluid/rock ratios (Bau, 1991) as the main factor that controlled the distribution of REE.

506

507 *7.2. Mechanism(s) of REY transport and origin of the Eu and Y anomalies*

508 As pointed out by Sallet et al. (2005), the positive PAAS-normalized Eu anomaly shown by

509 the Aouli fluorite (Eu/Eu* = 1.4-4.5; Fig. 4) could indicate either: (1) deposition from high-

510 temperature (>250°C) reducing fluids where Eu^{2+} dominates over Eu^{3+} (Möller et al., 1994,

511 1997; Bau, 1991), (2) inheritance from host rock dissolution at temperatures < 250°C, and/or

512 (3) chemical complexation reactions or adsorption effects.

513   Thermodynamic constraints indicate that under hydrothermal conditions, and at

514 temperature ranges similar to those that prevailed at the Aouli vein system (<250°C), all the

515 REE could be transported more efficiently as chloride and sulphate complexes rather than as

516 fluoride complexes (Migdisov and Williams-Jones, 2007, 2008; Migdisov et al., 2009).

517   Moreover, the scarcity of calcite and CO_2-bearing fluid inclusions suggests that CO_3^{2-}

518 was at best a minor complexing agent. More importantly, F^- and SO_4^{2-} anions would have not

519 constituted efficient ligands as the lack of solubility of barite, gypsum and fluorite would

520 have limited the concentration of these ligands in the ore-forming fluids to no more than a

521 few 100's ppm.

522   Accordingly, it is concluded that Cl^-, and to a much lesser extent CO_3^{2-} with possibly

523 variable but low amounts of F^- and SO_4^{2-} complexes controlled the hydrothermal mobilization

524 of the REE. Sorption of REE on mineral surfaces (Bau, 1996) is likely to have played only a

525 minor role, if any, because of the large size of the Aouli fluorite crystals which offers only a

526 small reactive specific surface area for sorption.

527   The distinctly positive Y_{PAAS} anomalies shown by the Aouli fluorite (Fig. 4), along with

528 the Y/Ho ratios of 25-186 (Table 1) that are higher than the chondritic Y/Ho ratios of 28

529 (Anders and Grevesse, 1989; McDonough and Sun, 1995; Irber, 1999), are suggestive of Y-

530 complexation, fluid interaction along the fluid path, remobilization and long distance

531 migration of the F-rich mineralizing fluid (Bau and Dulski, 1995; Wood, 1990a, b; Sallet et

532 al., 2005, Schwinn and Markl, 2005; Schönenberger et al., 2008). During migration toward

533 the site of deposition, intensive, high-temperature interaction of the mineralizing fluids with

534 the the plagioclase-bearing host rocks of the Aouli batholith and the uncoformably overlying

535 Triassic feldspar-rich arkoses, resulted in leaching of REY, which may explain the origin of

536 the prominent PAAS-normalized positive Eu anomalies (Fig. 4). The high thermal regime

537 (temperatures > 250°C) required to maintain the positive Eu anomaly, however, contrasts

538 with fluid inclusions data which indicate that the temperatures of the mineralizing fluids from

539 which the Aouli fluorite precipitated were substantially lower than 200°C (Table 4). We

540 suggest that the ore forming fluids acquired their REY characteristics during fluid-rock

541 interaction at higher temperatures deeper within the underlying granites and migrated to the

542 site of ore deposition prior to fluorite crystallization. A positive Eu anomaly inherited from

543 dissolution of the country host rocks seems unlikely since these latter (i.e., the Aouli

544 intrusions and the Triassic arkoses) exhibit salient negative rather than positive Eu anomalies

545 (Fig. 4).

546 *7.3. Physico-chemical conditions and sources of the ore fluids*

547 The microthermometry data of the fluorite hosted inclusions from the four vein systems show

548 that overall there is a large range of temperatures and salinities. However in Figure 12, the

549 salinity vs homogenization temperatures show that at each site the fluids are discrete from

550 each other. The highest salinity fluids are from veins hosted in the granites (Sidi Ayad and

551 Ansegmir), and the lowest with veins in the Cambro-Ordovician schists (Aouli and Sidi

552 Said). The lower temperatures are from the more eastern deposits and the higher temperatures

553 from those in the west. Thus the lithological association seen for salinity does not hold for

554 temperature. The major fluid components, NaCl and $CaCl_2$ were determined from the ice and

555 hydrohalite temperatures as shown in Figure 13. The most Ca-rich fluid, and highest

556 temperature and salinity is from Ansegmir vein system located in granite and the most

557 westerly. The Sidi Said vein system, more to the east in the Cambro-Ordovician schists has a

558 lower range of Ca/Na ratios almost to pure NaCl fluids. The remaining two vein systems

559 further to the east have inclusions which plot on or very close to the H_2O-NaCl axis of the

560 ternary diagram and therefore the least $CaCl_2$ in the fluid. We can therefore infer that the

561 fluid system involves the mixing of fluids where the $CaCl_2$/NaCl ratio is quite different. The

562 more calcic fluid dominates in the west and the more sodic fluid to the east.

563 The coexistence of hydrates and ice at temperatures below -21.2°C is only possible if

564 there are significant anions such as HCO_3^- and SO_4^{2-} in the fluids in addition to Cl^- (Banks

565 and Russell, 1992). However we believe these low temperatures are an analytical artefact and

566 that additional anions are not present in significant amounts. The presence of barite and

567 carbonate lithologies would limit their concentration to only a few 10's of ppm. Thus, the

568 bulk composition of these saline fluids approximates to H_2O-NaCl-$CaCl_2$ with variable

569 NaCl/(NaCl+ $CaCl_2$) ratios (Fig. 13) and unknown amounts of other cations. These fluid

570 compositions are similar to those of present-day oil-field brines, Mississippi Valley-type

571 mineralizing fluids where Ca-rich and Na-rich fluids are also commonly observed (Carpenter

572 et al., 1974; Haynes and Kesler, 1987; Leach and Sangster, 1993), and fluids related to

573 "peridiapiric" Pb-Zn ± F ± Ba ± Fe deposits (Sheppard et al., 1996; Bouabdellah et al., 2014).

574 The timing of mineralization precludes the involvement of any magmatic fluids from

575 the Variscan intrusions for the four mineralized vein systems or from the metamorphic

576 schists. The saline Na-Ca fluid compositions are therefore indicative of basinal sources (i.e.,

577   saliferous Permian-Triassic and the Lias-Dogger sequences), thereby supporting an

578   epigenetic hydrothermal basin-derived fluid model. However, the granitic intrusions would

579   still be associated by albitisation of feldspars, for example, to make a more Ca-rich fluid with

580   the release of REE and Ba. Modification of the fluid composition by brines interacting with

581   the Cambro-Ordovician schists (Gilg et al, 2006) is also possible.

582   The net distinction between the fluid inclusion populations could reflect either the

583   involvement of chronologically separated basin-derived mineralizing events, or temporal

584   evolution related to a single hydrothermal system. The similarity of the mineral assemblages

585   forming the different vein systems, irrespective of their strike, coupled with the oscillatory

586   zoning exhibited by some fluorite crystals (Fig. 3D) reflects episodic fluctuation in fluid

587   composition rather than involvement of chronologically separated mineralizing events.

588   More interestingly, the salinity versus vein system plot of Figure 15 show a linear

589   salinity distribution that is interpreted to represent a binary mixing line, suggestive of fluid

590   mixing and fluid-rock interaction between two distinct brine types (F_1, F_2) having contrasting

591   salinities, and Mg/(Ca + Mg) ratios. The statistical distribution of T_h values and related

592   salinities which exhibit two distinct peaks at ~120°C and ~140°C, and 17 and 23 wt % NaCl

593   equiv, respectively (Fig. 11), constitutes additional evidence for more than one fluid. The F_1

594   end-member may correspond to a high-temperature and high-salinity NaCl-CaCl$_2$-REE-rich,

595   deep-seated, ascending brine (~24 wt % NaCl equiv, up to 10 wt % CaCl$_2$), whereas the

596   second end-member F_2 corresponds to a lower-temperature and lower-salinity NaCl-rich (~14

597   wt % NaCl equiv), CaCl$_2$-REE-depleted, diluted, formation water. The more saline and

598   CaCl$_2$–rich fluids are related to the location of mineralization in or close to the granitic

599   intrusions, whereas the less saline and NaCl-rich fluids are associated with mineralization in

600   the Cambro-Ordovician schists. This distinction does not hold for the fluid temperatures but

601   may be related to the deposits in the west (containing both high and low salinity fluids) being

602   at deeper structural levels than those to the NE (which also contain both salinity fluids).

603   Mixing probably occurred at the interface basement-cover unconformity, as proposed for

604   many fluorite-barite ± sulphides hydrothermal deposits worldwide (Grandia et al., 2003;

605   Staude et al., 2009; 2011; Aquilina et al., 2011).

606

607   *7.4. Controls on fluid flow, fluid-rock interaction and source of sulphur and metals*

608   Field relationships indicate that the bulk of the structurally controlled fluorite-barite

609   mineralized veins are confined to the E-W and ENE-trending fault structures within which

610   brecciation and open space filling repeatedly occurred. Such intimate relationships to major

611   tectonic structures (Fig. 1) suggest that E-W (Tethyan dominance) and ENE-trending brittle

612   structures (Atlantic dominance; Ellouz et al., 2003) were the major pathways that focused

613   fluid flow. In addition to creating fracture permeability, brittle tectonic deformation may have

614   provided escape routes that allowed fluids residing in the basement to ascend into the cover

615   rocks.

616   During their migration, extensive chemical interaction between the migrating

617   mineralizing brines and the traversed aquifers occurred along their flow paths resulting in

618   selective leaching of, among other elements, REE, Sr, F, and Ba from the country rocks. At

619   the Aouli district, potential source rocks for these elements include the metamorphic and

620   igneous rocks of the Variscan crystalline basement, and the unconformably overlying lower

621   Triassic basal arkoses. The Liassic carbonates are excluded since the age of mineralization is

622   inferred to be older than the Jurassic carbonates (*see section age of mineralization*). In

623   support of this conclusion, the Sr isotope ratios for the fluorite and barite separates (^{87}Sr/^{86}Sr

624   = 0.708173-0.712293, avg = 0.710945, n = 22) are significantly higher than those for the

625   whole-rock Liassic carbonates (^{87}Sr/^{86}Sr = 0.707867-0.708140; avg = 0.708010, n = 3) whose

626   Sr isotopic signature is supposed to be representative of the Jurassic seawater (0.7075 to

627   0.7070; Burke et al., 1982; McArthur et al., 2001). Instead, the recorded Sr isotope ratios are

628   suggestive of interaction with ^{87}Sr-enriched fluids and that the Sr carried within the

629   hydrothermal solutions was not derived from the Liassic carbonate rocks, constraining

630   thereby the age of mineralization prior to Liassic time.

631   More interestingly, on a ^{87}Sr/^{86}Sr versus 1000/Sr covariation diagram, the Sr data plot

632   along a curvilinear array (Trend I; Fig. 9) interpreted to represent fluid mixing between two

633   end-members: (1) a Sr-rich fluid source with relatively low ^{87}Sr/^{86}Sr ratios, and (2) a Sr-poor

634   fluid source enriched in ^{87}Sr with ^{87}Sr/^{86}Sr ratios up to 0.7185 (Table 3). Consistent with fluid

635   inclusion data, the Sr-poor radiogenic end-member (F_1), whose ^{87}Sr/^{86}Sr ratios are similar to

636   those characterizing some Canadian Shield brines (^{87}Sr/^{86}Sr = 0.706-0.755; Negrel and

637   Casanova, 2005; Gromek et al., 2012), is interpreted to represent deep-seated, ascending,

638   seawater-derived brine that has equilibrated with Late Variscan crystalline basement rocks,

639   whereas the second Sr-rich unradiogenic end-member (F_2) is interpreted to represent Permian

640   to Triassic stagnant formation and/or meteoric water. Mixing between basement brines and

641   meteoric waters at the basement-cover interface has been invoked for the genesis of many

642   Variscan vein-type fluorite-barite-sulphide deposits scattered throughout Central and Western

643   Europe (Munoz et al., 2005; Schwinn and Markl, 2005; Schwinn et al., 2006, Castorina et al.,

644   2008; Piqué et al., 2008; Sanchez et al., 2009; Staude et al., 2009; 2011; Dill and Weber,

645   2012).

646   The origin of Ca enrichment remains controversial (Hanor, 1994) and could potentially

647   be attributed to either albitization of plagioclase, dolomitization and leaching of carbonate

648   strata, and/or dissolution of the Triassic evaporites, or a combination of all these processes.

649   The high Sr contents of barite (Table 3) are compatible with an evaporative source as Ca and

650   Sr are easily transported in saline solutions (Holland and Malinin, 1979). In addition to this

651   evaporative source, the positive Eu_{PAAS} anomalies shown by the Aouli fluorite separates (Fig.

652   4) along with the rare occurrence of carbonate strata suggest selected leaching of Eu mainly

653   from the plagioclase-bearing rocks (e.g., Late Variscan granitoids and in a lesser extent the

654   overlying Triassic arkoses). In addition to providing Ca by breakdown of feldspars, the

655   Triassic arkosic rocks and the underlying Late Variscan granitoids would have been the most

656   probable sources of Sr, F, and Ba as already suggested by Sr isotope compositions. In this

657   regards, the main mineral species contributing Sr, Ba and F are plagioclase, K-feldspars, and

658   mica with the two latter yielding Sr with high $^{87}Sr/^{86}Sr$ because of their high Rb contents

659   (Chaudhuri and Clauer, 1993).

660   The sulphur source can be constrained by the overall uniform distribution of $\delta^{34}S_{barite}$

661   values in the range of +11 to +13‰ (avg = +12‰, n = 9) which reflects the homogeneity of

662   the aqueous sulphate source in the mineralizing fluid, and indicates that intensive parameters

663   such as temperature, pH, f_{O2}, source reservoirs and oxidation state of fluid did not

664   significantly affect the sulphur isotope composition of barite. The recorded data are, thus,

665   consistent with derivation of sulphur from Permian to Triassic seawater sulphate (11-14%;

666   Claypool et al., 1980; Strauss, 1997). During barite deposition, sulphate may have been

667   derived from connate seawater, evaporative concentrated seawater, or from fluids that

668   dissolved gypsum from the Permian-Triassic evaporite-bearing red beds.

669

670   **8. Genetic model: concluding remarks**

671   Paleogeographic reconstructions indicate that the overburden in the Upper Moulouya District

672   never exceeded 2 km (Beauchamp et al., 1996; Ellouz et al., 2003) constraining thereby the

673   maximum burial temperature in the range of <85°C, assuming a mean geothermal gradient of

674   30°C/km and a surface temperature of 25°C. These burial temperatures are substantially

675   lower than the fluid inclusion homogenization temperatures. The higher temperatures require

676   either the existence of an abnormally high geothermal gradient or fluids expelled from deeper

677 levels of the nearby sedimentary basins. Field relationships along with apatite fission age
678 dating indicate that the Aouli fluorite-barite ± sulphides mineralization occurred during the
679 Permian-Triassic which regionally (i.e., Western Mediterranean Basin), this interval coincides
680 with the rift and pre-rift stages of Pangea and Central Atlantic opening (Irving, 1977; Torcq et
681 al., 1997; Muttoni et al., 2003, Martins et al., 2008). Subsequent crustal thinning and an
682 increased geothermal gradient could have resulted in the development of small-scale
683 convection cells that acted as the source of heating and driving mechanism to move the
684 mineralizing fluids toward shallower depths. In this respect, hydrological modelling
685 performed by Staude et al. (2009) showed that extension can release, through decompression
686 of over-pressured rocks and/or heating, sufficient amounts of fluids in the order of 10^{-3} to 10^{-4}
687 km^3 fluid per km^2 crustal column to form an economic ore deposit.

688   The REYs along with fluid inclusion and Sr isotope data exclude any direct sourcing of
689 fluids for the fluorite-barite ± sulphides mineralization from the spatially associated Late
690 Variscan granitic intrusions. However, these intrusions are high heat producing granites
691 (HHP) and radioactive heat from solidified HHP granites has been shown to be capable of
692 generating hydrothermal convection of sufficient magnitude to form metallic deposits (Fehn,
693 1985; Bjørlykke et al., 1991; Spirakis and Heyl, 1996). Our geochemical data along with
694 those available in literature (Dahire, 2004) indicate that the average U and Th contents of the
695 Aouli granitic rocks are among the highest values recorded for the Moroccan Late Variscan
696 granitoids, and fit within the range of values characterizing typical HHP granites (> 6 ppm U
697 and/or > 25 ppm Th; O'Connor, 1986). Accordingly, we suggest therefore that such granites
698 may have represented a potential thermal source for the basinal fluids

699   From fluid inclusion data, REYs, and Sr isotopic constraints it is appears that mixing of
700 two contrasting fluids (i.e., F_1, F_2), triggered the deposition of the Aouli fluorite-barite ±
701 sulphides mineralization by cooling and/or decreasing the solubility of F^- by mixing with the
702 Ca-rich fluid. The F_1, radiogenic, high-temperature and high-salinity, $NaCl$-$CaCl_2$-REE-rich
703 end-member may correspond to an ascending deep-seated fluid that was equilibrated with
704 Late Variscan crystalline basement rocks at least 5-7 km depth, which occurred in the
705 Pyrenees (Banks et al, 1991; McCaig et al, 2000) and Morocco (Esseraj et al., 2005), whereas
706 the F_2, unradiogenic, lower temperature and lower salinity, $CaCl_2$-REE-depleted end-member
707 may represent Permian to Triassic formation and/or meteoric water. Extension would have
708 opened fractures in the granites thus providing high fluid flow pathways for ascending fluids.
709 Mixing of the two fluid components occurred at the unconformable basement-cover interface.

710   Seismic data shows the occurrence of a low velocity zone in the middle crust below the

711 Upper Moulouya District (Schwarz and Wigger, 1988; Jacobshagen et al., 1988, Ayarza et

712 al., 2005). The existence of such a zone has been interpreted to be related to the existence of a

713 fluid enrichment zone due to the exhumation of the Upper Moulouya District (Ayarza et al.,

714 2005). Hence, it appears that crustal dewatering during Permian-Triassic exhumation

715 produced the lower velocity zone, and that the resulting ascending fluid which ultimately

716 mixed with the stagnant formation and/or meteoric waters could have been responsible for

717 the genesis of the fluorite-barite ± sulphides mineralization.

718   The source of fluorine, a frequently debated issue for many fluorite hydrothermal

719 deposits worldwide, remains, however, controversial. At the Upper Moulouya District, fluid

720 inclusion microthermometric measurements along with REE and Sr isotopic constraints

721 preclude direct involvement of rift-related gaseous HF released from degassing alkaline

722 magmas. Rather, these data suggest leaching of fluorine from the Aouli Late Variscan granitic

723 batholith. Indeed, petrographic and geochemical studies show that the Aouli batholith is a

724 multiphase compositionally complex intrusion whose petrographic units crystallized from

725 shoshonitic to high-K calc-alkaline magmas (Dahire, 2004). In these two petrographic

726 associations, the F and Ba contents are as high as 715 and 1972 ppm; respectively (Dahire,

727 2004, and the present study). These concentrations are high enough to suggest that the

728 alkaline granite could have constituted potential F source for the Aouli fluorite-barite

729 mineralization by hydrothermal alteration of biotite to chlorite. The down flow of the

730 mineralizing brine would have been focused along the alkaline granitic units.

731

740

741

742

743

References

Anders, E., Grevesse, N., 1989. Abundances of the elements: meteoric and solar. Geochimica et Cosmochimica Acta 53, 197-214.

Annich, M., Rahhali, M., 2002. Gisement de plomb de Zeida. In: Barodi E-B, Watanabe Y, Mouttaqi A, Annich M (eds) Méthodes et techniques d'exploration minière et principaux gisements au Maroc. JICA/BRPM Project, pp 179-183.

Aquilina, L., Boulvais, P., Mossmann, J.R., 2011. Fluid migration at the basement/sediment interface along the margin of the Southeast basin (France): implications for Pb-Zn ore formation. Mineralium Deposita 46, 959-979.

Ayarza, P., Alvarez-Lobato, F., Teixel, A., Arboleya, M.L., Tesón, E., Julivert, M., Cherroud, M., 2005. Crustal structure under the central High Atlas mountains (Morocco) from geophysical and gravity data. Tectonophysics 400, 67-84.

Bakker, R., 2003. Package FLUIDS 1. Computer programs for analysis of fluid inclusion data and for modeling bulk fluid properties. Chemical Geology 194, 3-23.

Banks, D.A., Davies, G.R., Yardley, B.W.D., McCaig, A.M., Grant, N.T., 1991. The chemistry of brines in an Alpine thrust system from the Pyrenees: An application of fluid inclusion analyses to the study of fluid behavior in orogenesis. Geochim. et Cosmochim. Acta 55, 1021-1030.

Banks, D.A., Russell, M.J., 1992. Fluid mixing during ore deposition at the Tynagh base-metal deposit, Ireland. Eur. J. Mineral 4, 921-931.

Barbero, L., Jabaloy, A., Gómez-Ortiz, D., Pérez-Peña, J.V., Rodríguez-Peces, M.J., Tejero, R., Estupiñan, J., Azdimousa, A., Vázquez, M., Asebriy, L., 2011. Evidence for surface uplift of the Atlas Mountains and the surrounding peripheral plateaux: Combining apatite fission-track results and geomorphic indicators in the Western Moroccan Meseta (coastal Variscan Paleozoic basement). Tectonophysics 502, 90-104.

Bau, M., 1991. Rare-earth element mobility during hydrothermal and metamorphic fluid-rock interaction and the significance of oxidation state of europium. Chemical Geology 93, 219-230.

Bau, M., Dulski, P., 1995. Comparative study of yttrium and rare-earth element behaviour in fluorine-rich hydrothermal fluids. Contrib Mineral Petrol 119, 213–223.

Bau, M., Romer, R.L., Lüders, V., Dulski, P., 2003. Tracing element sources of hydrothermal mineral deposits: REE and Y distribution and S–Nd–Pb isotopes in fluorite from MVT deposits in the Pennine Orefield, England. Mineralium Deposita 38, 992-1008.

777 Bau, M., 1996. Controls on the fractionation of isovalent trace elements in magmatic and
778   aqueous systems: evidence from Y/Ho, Zr/Hf, and the lanthanide tetrad effect. Contrib.
779   Mineral. Petrol. 123, 323-333.

780 Beauchamp, W., Barazangi, M., Demnati, A., El Alji, M., 1996. Intracontinental rifting and
781   inversion: Missour Basin and Atlas Mountains, Morocco. AAPG Bull 80, 1459-1482.

782 Bjørlykke, A., Sangster, D.F., Fehn, U., 1991. Relationship between high heat producing
783   (HHP) granites and stratabound lead-zinc deposits. In: Pagel M, Leroy M (eds) Source,
784   transport, and deposition of metals. Balkema, Rotterdam, pp 257-260.

785 Bodnar, R.J., Bethke, P.M., 1984. Systematics of stretching of fluid inclusions I: Fluorite and
786   sphalerite at 1 atmosphere confining pressure. Economic Geology 79, 141-161.

787 Bodnar, R.J., 2003. Reequilibration of fluid inclusions, in Samson, I., Anderson, A., and
788   Marshall, D., eds., Fluid Inclusions: Analysis and Interpretation. Mineral Assoc Canada
789   Short Course 32, pp. 213-230.

790 Bouabdellah, M., Banks, D., Klügel, A., 2010. Comments on "A late Triassic ^{40}Ar/^{39}Ar age
791   for the El Hammam high-REE fluorite deposit (Morocco): mineralization related to the
792   Central Atlantic Magmatic Province? Mineralium Deposita 45, 729-731.

793 Bouabdellah, M., Castorina, F., Bodnar, R.J., Banks, D., Jébrak, M., Prochaska, W., Lowry,
794   D., Klügel, A., Hoernle, K., 2014, Petroleum migration, fluid mixing, and halokinesis as
795   the main ore-forming processes at the peridiapiric Jbel Tirremi fluorite-barite
796   hydrothermal deposit, Northeastern Morocco. Economic Geology 108, 1223-1256.

797 Burke, W.H., Denison, R.E., Hetherington, E.A., Koepinck, R.B., Nelson, H.F., Otto, J.B.,
798   1982. Variation of seawater ^{87}Sr/^{86}Sr throughout Phanerozoic time. Geology 105, 16-519.

799 Canals, A., Cardellach, E., Rye, D.M., Ayora, C., 1992. Origin of the Atrevida vein
800   (Catalonian Coastal Ranges, Spain): mineralogy, fluid inclusion and stable isotope study.
801   Economic Geology 87, 142-153.

802 Canals, A., Cardellach, E., 1993. Strontium and sulphur isotope geochemistry of low
803   temperature barite–fluorite veins of the Catalonian Coastal Range (NE Spain): a fluid
804   mixing model and geochemistry constraints. Chemical Geology 104, 269-280.

805 Carignan, J., Hild, P., Mevelle, G., Morel, J., Yeghicheyan, D., 2001. Routine analyses of
806   trace elements in geological samples using flow injection and low pressure on-line liquid
807   chromatography coupled to ICP-MS: a study of reference materials BR, DR-N, UB-N,
808   AN-G and GH. Geostand. Newsl. J. Geostand. Geoanal 25(2-3), 287-198.

809   Carpenter, A.B., Trout, M.L., Pickett, E.E., 1974. Preliminary report on the origin and
810   chemical evolution of lead-and-zinc-rich oil field brines in central Mississippi. Economic
811   Geology 69, 1191-1206.

812   Castorina, F., Masi, U., Padalino, G., Palomba, M., 2008. Trace-element and Sr-Nd isotopic
813   evidence for the origin of the Sardinian fluorite mineralization (Italy): Applied
814   Geochemistry 23, 2906-2921.

815   Chaudhuri, S., Clauer, N., 1993. Strontium isotopic composition and potassium and rubidium
816   contents of formation waters in sedimentary basins: clues to the origin of the solutes.
817   Geochimica et Cosmochimica Acta 57, 429-437.

818   Cheilletz, A., Gasquet, D., Filali, F., Archibald, D.A., Nespolo, M., 2010. A late Triassic
819       $^{40}Ar/^{39}Ar$ age for the El Hammam high-REE fluorite deposit (Morocco): mineralization
820   related to the Central Atlantic Magmatic Province? Mineralium Deposita 45, 323-329.

821   Clauer, N., Jeannette, D., Tisserant, D., 1980. Datation isotopique des cristallisations
822   successives du socle cristallin et cristallophyllien de la haute Moulouya (Maroc
823   hercynien), Geol Rundsch 68, 63-83.

824   Claypool, G.E., Holser, W.T., Kaplan, T.R., Sakai, H., Zak, I., 1980. The age curves of sulfur
825   and oxygen isotopes in marine sulfate and their mutual interpretations. Chemical Geology
826   28, 199-260.

827   Crawford, M.L., 1981. Phase equilibria in aqueous fluid inclusions. In: Hollister, L.S.,
828   Crawford, M.L., (eds) Fluid Inclusions: Applications to Petrology. Mineralogical
829   Association of Canada Short Course Handbook 6, pp 75-100.

830   Dagallier, G., 1983. Contribution à l'étude de l'environnement de concentrations plombo-
831   zincifères (et métaux connexes) liées aux strates. Unpublished PhD thesis, Nancy
832   University (France), p 273.

833   Dahire, M., 2004. Le complexe plutonique de la Haute Moulouya (Meseta oriental, Maroc) :
834   Evolution pétrologique et structurale. Unpublished PhD thesis, Mohamed Ben Abdellah
835   University, Fès (Morocco), p 322.

836   Davis, D.W., Lowenstein, T.K., Spencer, R.J., 1990. Melting behavior of fluid inclusions in
837   laboratory-grown halite crystals in the systems NaCl- H_2O, NaCl-KC1-H_2O, NaCl-$MgCl_2$-
838   H_2O, and NaC1-$CaCl_2$-H_2O: Geochimica et Cosmochimica Acta 54, 591-601.

839   Dill, H.G., Hansen, B.T., Weber, B., 2011. REE contents, REE minerals and Sm/Nd isotopes
840   of granite- and unconformity-related fluorite mineralization at the western edge of the
841   Bohemian Massif: with special reference to the Nabburg-Wölsendorf district, SE
842   Germany: Ore Geology Reviews 40, 132-148.

843 Diot, H., Bouchez, J.L., 1989. Les granitoïdes hercyniens de la Haute Moulouya (Maroc) :
844   leur structure primaire déduite de l'ASM. Indications sur leur mise en place. Bull Soc
845   Geol France 4, 387-394.

846 Dubois, M., Marignac, C., 1997. The H_2O-NaCl-$MgCl_2$ ternary phase diagram with special
847   application to fluid inclusion studies. Economic Geology 92, 114-119.

848 Duggen, S., Hoernle, K., Hauff, F., Klügel, A., Bouabdellah, M., Thirlwall, M.F., 2009. Flow
849   of Canary mantle plume material through a subcontinental lithospheric corridor beneath
850   Africa to the Mediterranean. Geology 37(3), 283-286.

851 Ellouz, N., Patriat, M., Gaulier, J.M., Bouatmani, R., Saboundji, S., 2003. From rifting to
852   Alpine inversion: Mesozoic and Cenozoic subsidence history of some Moroccan basins,
853   Sedim. Geol. 156, 185-212.

854 Emberger, A., 1965. Caractères polygénétiques des minéralisations plombifères de la Haute
855   Moulouya (gisements d'Aouli, Mibladen et Zeïda, Maroc). C. R. Acad. Sci. Paris, t. 260.
856   Groupe 9, pp. 3433-3436.

857 Emberger, A., 1965. éléments pour une synthèse métallogénique du district plombifère de la
858   Haute Moulouya. In : Colloque sur des gisements stratiformes de Plomb, Zinc et
859   Manganèse du Maroc 1962. Notes Mém Serv Géol Maroc 181, pp 235-238.

860 Essarraj, S., Boiron, M-C., Cathelineau, M., Banks D.A., Benharref, M., 2005. Penetration of
861   surface evaporated brines into the Proterozoic basement and deposition of Co and Ag at
862   Bou Azzer (Morocco): Evidence from fluid inclusions. Journal of African Earth Sciences
863   41, 25-39.

864 Fehn, U., 1985. Post magmatic convection related to high heat production of granites of
865   southwest England: a theoretical study. In: High heat production (HHP) granites,
866   hydrothermal circulation and ore genesis. Institute of Mining and Metallurgy, London, pp
867   99-113.

868 Filali, F,. 1996. Etude pétro-structurale de l'encaissant métamorphique de la boutonnière
869   d'Aouli-Mibladen (Haute Moulouya, Maroc): conséquences sur la géodynamique
870   hercynienne au Maroc. Unpublished PhD thesis, Muséum National d'Histoire Naturelle,
871   Paris (France), p 174.

872 Filali, F., Guiraud, M., Burg, J.P., 1999. Nouvelles données petro-structurales sur la
873   boutonnière d'Aouli (Haute Moulouya): leurs conséquences sur la géodynamique
874   hercynienne du Maroc. Bulletin de la Société Géologique de France 4, 435-450.

875 Gagnon, J.E., Samson, I.M., Fryer, B.J., Williams-Jones, A.E., 2003. Compositional
876   heterogeneity in fluorite and the genesis of fluorite deposits: insights from LA-ICP-MS
877   analysis. The Canadian Mineralogist 41, 365-382.

878 Ganzeev, A., Mitiaev, A., 1978. Caractéristiques métallogéniques des roches éruptives de la
879   Haute Moulouya. Mines, Géologie et Energie 44,127-130.

880 Ghorbal, B., Bertotti, G., Foeken, J., Andriessen, P., 2008. Unexpected Jurassic to Neogene
881   vertical movements in 'stable' parts of NW Africa revealed by low temperature
882   geochronology. Terra Nova 20, 355-363.

883 Gilg, H.A., Boni, M., Balassonne, G., Allen, C.R., Banks, D.A., Moore, F., 2006. Marble-
884   hosted sulphide ores in the Angouran Zn-(Pb-Ag) deposit, NW Iran: interaction of
885   sedimentary brines with a metamorphic core complex. Mineralium Deposita 41, 1-16.

886 Gleeson, S.A., Wilkinson, J.J., Stuart, F.M., Banks, D.A., 2001. The origin and
887   evolution of base metal mineralising brines and hydrothermal fluids, South Cornwall,
888   UK. Geochimica et Cosmochimica Acta 65, 2067-2079.

889 Goldstein, R.H., Reynolds, T.J., 1994. Systematics of fluid inclusions in diagenetic minerals.
890   SEPM Short C 31, pp 1-199.

891 Grandia, F., Cardellach, E., Canals, A., Banks, D.A., 2003. Geochemistry of the fluids related
892   to epigenetic carbonate-hosted Zn-Pb deposits in the Maestrat Basin, Eastern Spain: fluid
893   inclusion and isotope (Cl, C, O, S. Sr) evidence. Economic Geology 98, 933-954.

894 Gromek, P., Gleeson, S.A., Simonetti, A., 2012.A basement-interacted fluid in the N81
895   deposit, Pine Point Pb-Zn District, Canada: Sr isotopic analyses of single dolomite
896   crystals. Mineralium Deposita 47(7), 749-754.

897 Hanor, J.S.,1994, Origin of saline fluids in sedimentary basins. In: Parnell J (ed) Geofluids:
898   origin and migration of fluids in sedimentary basins. Geol Soc London, Spec Publ 78,
899   151–174.

900 Harmand C, Cantagrel JM (1984) Le volcanisme alcalin Tertiaire et Quaternaire du Moyen
901   Atlas (Maroc):chronologie K/Ar et cadre géodynamique. Journal of African Earth
902   Sciences 2:51-55

903 Haynes FM, Kesler SE (1987) Chemical evolution of brines during Mississippi Valley-type
904   mineralization: evidence from East Tennessee and Pine Point. Economic Geology 82:53–
905   71

906 Holland HD, Malinin SD, 1979, The solubility and occurrence of non-ore minerals. In:
907   Barnes HL (eds) Geochemistry of hydrothermal ore deposits. 2nd edition, New York, John
908   Wiley, pp 461-508

909 Hoepffner C, Rachid Houari M, Bouabdelli M (2006) Tectonics of the North African
910   Variscides (Morocco, western Algeria): an outline. C. R. Geosciences 338:25-40

911 Irber W (1999) The lanthanide tetrad effect and its correlation with K/Rb, Eu/Eu*, Sr/Eu,
912   Y/Ho, and Zr/Hf of evolving peraluminous granite suites. Geochimica et Cosmochimica
913   Acta 63:489-508

914 Irving E (1977) Drift of the major continental blocks since the Devonian. Nature 270:304-309

915 Jacobshagen VH, Gorler K, Giese P (1988) Geodynamic evolution of the Atlas System
916   (Morocco). In: Jacobshagen VH (ed) The Atlas System of Morocco.Springer-Verlag,
917   Berlin Heidelberg New York, pp 481-499

918 Jébrak M (1984) Contribution à l'histoire naturelle des filons (F-Ba) du domaine varisque
919   Français et marocain. Essai de caractérisation structurale et géochimique des filons en
920   extension et en décrochement. Unpublished PhD thesis, Document du Bureau de
921   Recherche Géologique et Minière 99, p 510

922 Jébrak M, Smejkal V, Albert D (1985) Rare earth and isotopic geochemistry of the fluorite-
923   barite vein deposits from the western Rouergue district (France). Economic Geology
924   80:2030-2034

925 Jébrak M, Marcoux E, Nasloubi M, Zahraoui M (1998) From sandstone- to carbonate-hosted
926   stratabound deposits: an isotope study of galena in the Upper-Molulouya district
927   (Morocco). Mineralium Deposita 33: 406-415

928 Jébrak M, El Wartiti M, Marcoux E, Zahraoui M (2011) The Bouznika Cambrian barite
929   deposit (Morocco), an early mineralization on the Iapetus margin. Journal of African Earth
930   Sciences 60 (3): 53-62

931 Johnson CA, Cardellach E, Tritlla Hanan BB (1996) Cierco Pb-Zn vein deposits: isotopic and
932   fluid inclusion evdience for formation during the Mesozoic extension in the Pyrenees of
933   Spain. Economic Geology 91: 297-306

934 Klitgord KD, Schouten H (1986) Plate kinematics of the central Atlantic. In: Vog PR,
935   Tucholke BE (eds) The geology of North America. Vol. M. The Western North Atlantic
936   Region, Geological Society of America, Boulder, pp. 351-377

937 Lawler JP, Crawford M.L (1983) Stretching of fluid inclusions resulting from a low-
938   temperature microthermometric technique: Economic Geology 78:527-529

939 Leach DL, Sangster DF (1993) Mississippi Valley-type lead-zinc deposits. In: Kirkham RV,
940   Sinclair WD, Thorpe RI, Duke JM (eds) Mineral deposit modeling. Geol Assoc Can Spec
941   Pap 40, pp 289-314

942 Lhégu J, Touray J.C (1980) Les gisements français filoniens et stratiformes de fluorine et
943   barytine. 26th International Geological Congress, Paris, July 7-17: Bulletin du Centre de
944   Recherche et d'Exploration Production Elf-Aquitaine 3, pp.277-334

945 Martins LT, Madeira J, Youbi N, Munhá, Mata J, Kerrich R (2008) Rift-related magmatism
946   of the Central Atlantic magmatic province in Algarve, Southern Portugal. Lithos 101:102-
947   124

948 McArthur JM, Howarth RJ, Bailey TR (2001) Strontium isotope stratigraphy: Lowess
949   Version 3: Best-fit to the marine Sr-isotope curve for 0 to 509 Ma and accompanying
950   look-up table for deriving numerical age. Journal of Geology 109:155–170

951 McCaig A.M., Tritlla, J., Banks, D.A., 2000. Fluid mixing and recycling buring Pyrenean
952   thrusting: Evidence from fluid inclusion halogen ratios. Geochim. et Cosmochim. Acta 64,
953   3395-3412.

954 McDonough WFM, Sun SS (1995) The composition of the Earth. Chemical Geology
955   120:223-253

956 McLennan SM (1989) Rare earth elements in sedimentary rocks: influence of provenance and
957   sedimentary processes. In: Lipin BR, McKays GA (eds) Rare earth elements. Rev Mineral
958   21, pp.169-200

959 Migdisov AA, Williams-Jones AE (2007) An experimental study of the solubility and
960   speciation of neodymium (III) fluoride in F-bearing aqueous solutions: Geochimica et
961   Cosmochimica Acta 71:3056-3069

962 Migdisov, A.A., and Williams-Jones, A.E., 2008, A spectrophotometric study of Nd(III),
963   Sm(III) and Er(III) complexation in sulfate-bearing solutions at elevated temperatures.
964   Geochimica et Cosmochimica Acta 72:5291-5303

965 Migdisov AA, Williams-Jones AE, Wagner T (2009) An experimental study of the solubility
966   and speciation of the rare earth elements (III) in fluoride- and chloride-bearing aqueous
967   solutions at temperatures up to 300°C. Geochimica et Cosmochimica Acta 73:7087-7109

968 Möller P, Parekh PP, Schneider HJ (1976) The application of Tb/Ca-Tb/La abundance ratios
969   to problems of fluorite genesis. Mineralium Deposita 11:111-116

970 Möller P, Giese U, Dulski P (1994a) Behaviour of REE in alteration processes of granites. In:
971   Seltman R, Kämpf H, Möller P (Eds), Metallogeny of collisional orogens. Czech
972   Geological survey, Prague, pp 368-374

973 Möller P, Stober I, Dulski P (1997) Seltenerdelement-,Yttrium-Gehalte und Bleiisotope in
974   Thermal- und Mineralwässern des Schwarzwaldes. Zeischrift der fachsektion
975   Hydrogeology 3:118-131

976   Munoz M, Premo W.R, Courjault-Radé P (2005) Sm-Nd dating of fluorite from the
977   worldclasse Montroc fluorite deposit, southern Massif Central, France. Mineralium
978   Deposita 39:970-975

979   Muttoni G, Kent DV, Garzanti E, Brack P, Abrahamsen N, Gaetani M (2003) Early Permian
980   Pangea 'B' to Late Permian Pangea 'A'. Earth and Planetary Science Letters 215:379-394

981   Naji M (2004) Les minéralisations plombo-barytiques du district de la Haute Moulouya.
982   Contexte géologique, contrôle tectonique et modèle de mise en place : gisements d'Aoul-
983   Mibladen-Zeida. Unpublished PhD thesis, Mohammed V University, Rabat (Morocco), p
984   218

985   Negrel P, Casanova J (2005) Comparison of the Sr isotopic signatures in brines in the
986   Canadian and Fennoscandian shield. App. Geochem 20:749-766

987   Oakes CS, Bodnar RJ, Simonson JM (1990) The system $NaCl–CaCl_2–H_2O$. I. The vapor-
988   saturated ice liquidus. Geochimica et Cosmochimica Acta 54:603–610

989   O'Connor PJ (1986) Uranium mineralization in the Irish Caledonides. In: Andrew CJ, Crowe
990   RWA, Finlay S, Pennell WM, and Pyne JF (eds) Geology and genesis of mineral deposits
991   in Ireland. Irish Association for Economic Geology, pp. 154-175

992   Ouali H, Briand B, Bouchardon JL, El Maâtaoui M (2000) Mise en évidence d'un volcanisme
993   alcalin intraplaque d'âge Acadien dans la Meseta nord-occidentale (Maroc). C. R. Acad.
994   Sci. Paris 330:611–616

995   Ouarhache D, Charrière A, Charlot-Prat F, El Wartiti M (2012) Chronologie et modalities du
996   rifting triassico-liasique à la marge sud-ouest de la Téthys alpine (Moyen Atlas et Haute
997   Moulouya, Maroc) ; corrélation avec le rifting atlantique : simultanéité et diachronisme.
998   Bull. Soc. Geol. Fr. t. 183(3):233-249

999   Oukemeni D (1993) Géochimie, géochronologie (U-Pb) du pluton d'Aouli et comparaisons
1000   géochimiques avec d'autres granitoïdes hercyniens du Maroc par analyse discriminante.
1001   Unpublished PhD thesis, Québec University, Montréal (Canada), p 141

1002   Oukemeni D, Bourne JH (1994) Etude géochimique des granitoïdes du pluton d'Aouli, Haute
1003   Moulouya, Maroc. Journal of African Earth Sciences 17:429-443

1004   Oukemeni D, Bourne JH, Krogh TE (1995) Géochronologie U-Pb sur zircon du pluton
1005   d'Aoul, Haute Moulouya, Maroc. Bull. Soc. Géol. France 166:15-21

1006   Pearce NJG, Perkins WT, Westgate JA, Gortan MP, Jackson SE, Neal CR, et al (1997) A
1007   compilation of new and published major and trace element data for NIST SRM 610 and
1008   NIST SRM 612 glass reference materials. Geostand. Newsl. 21:115-144

1009 Pérez-Soba C,Villaseca C (2010) Petrogenesis of highly fractionated I-type peraluminous

1010   granites: La Pedriza pluton (Spanish Central System): Geologica Acta 8:131-149

1011 Pique A, Laville E (1993) L'ouverture de l'Atlantique central: un rejeu en extension des

1012   structures paléozoïques? Comptes Rendus Académie Sciences, Paris 317 (II):1325-1332

1013 Pique A, Canals A, Grandia F, Banks DA (2008) Mesozoic fluorite veins in NE Spain record

1014   regional base metal-rich brine circulation through basin and basement during extensional

1015   events. Chemical Geology 257:139–52

1016 Preece RKIII, Beane RE (1982) Contrasting evolutions of hydrothermal alteration in quartz

1017   monzonite and quartz diorite wall rocks at the Sierrita porphyry copper deposit, Arizona.

1018   Economic Geology 77: 1621-1641

1019 Rahhali M (2002a) Gisements stratiformes de Mibladen. In: Barodi E-B, Watanabe Y,

1020   Mouttaqi A, Annich M (eds) Méthodes et techniques d'exploration minière et principaux

1021   gisements au Maroc. Projet JICA/BRPM, pp 166-170

1022 Rahhali M (2002b) Gisements filoniens d'Aouli. In: Barodi E-B, Watanabe Y, Mouttaqi A,

1023   Annich M (eds) Méthodes et techniques d'exploration minière et principaux gisements au

1024   Maroc. Projet JICA/BRPM, pp 171-173

1025 Ricou L-E (1994) Tethys reconstructed: plates, continental fragments and their boundaries

1026   since 260 Ma from Central America to Southeastern Asia. Geodyn Acta 7(4):169-218

1027 Roedder E (1984) Fluid inclusions. Rev Mineral 12, p 644

1028 Rosé F (1987) Les types granitiques du Maroc hercynien. Unpublished PhD thesis, Paris VI

1029   University, Paris (France), p 381

1030 Saddiqi O, El Haimer F.Z, Michard A, Barbarand J, Ruiz G.M.H, Mansour E.M (2009)

1031   Apatite fission-track analyses on basement granites from south-western Meseta, Morocco:

1032   Paleogeographic implications and interpretation of AFT age discrepancies.

1033   Tectonophysics 475:29-37

1034 Sallet R, Moritz R, Fontignie D (2005) The use of vein fluorite as probe for paleofluid REE

1035   and Sr-Nd isotope geochemistry: The Santa Catarina Fluorite District, Southern Brazil.

1036   Chemical Geology 223:227-248

1037 Sanchez V, Corbella M, Fuenlabrada JM, Vindel E, Martin Crespo T (2006) Sr and Nd

1038   isotope data from the fluorspar district Asturias, northern Spain. Journal of Geochemical

1039   Exploration, 89:348-50

1040 Sánchez V, Vindel E, Martín-Crespo T, Corbella M, Cardellach E, Banks D (2009) Sources

1041   and composition of fluids associated with fluorite deposits of Asturias (N Spain).

1042   Geofluids 9:338-355

1043 Schönenberger J, Köhler J, Markl G (2008) REE systematics of fluorides, calcite and siderite
1044   in peralkaline plutonic rocks from the Gardar Province, South Greenland. Chemical
1045   Geology 247:16-35

1046 Schwarz G, Wigger PJ (1988) Geophysical studies of the Earth's crust and upper mantle in
1047   the Atlas system of Morocco. In: Jacobshagen VH (ed) The Atlas System of Morocco,
1048   Springer-Verlag, Berlin Heidelberg New York, pp 340-357

1049 Schwinn G, Markl G (2005) REE systematic in hydrothermal fluorite. Chemical Geology
1050   216:225-248

1051 Schwinn G, Wagner T, Baatartsogt B, Markl G (2006) Quantification of mixing processes in
1052   ore-forming hydrothermal systems by combination of stable isotope and fluid inclusion
1053   analyses. Geochimica et Cosmochimica Acta 70:965-982

1054 Sheppard SMF, Charef A, Bouhlel S (1996) Diapirs and Zn-Pb mineralization: a general
1055   model based on Tunisia (N. Africa) and Gulf Coast (USA) deposits. Society of Economic
1056   Geologists Special Publication 4, pp 230-243

1057 Sizaret S, Marcoux E, Jébrak M, Touray JC (2004) The Rosignol fluorite vein, Chaillac,
1058   France: multiphase hydrothermal activity and intra-vein sedimentation. Economic
1059   Geology 99:1107-1122

1060 Spirakis CS, Heyl AV (1996) Fracturing radioactive basement rocks as the energy source to
1061   drive mineralization in the Upper Mississippi Valley zinc-lead district. In: Sangster DF
1062   (ed) Carbonate-hosted Lead-Zinc Deposits. Society of Economic Geology, Special
1063   Publication 4, pp 390-399

1064 Staude S, Bons PD, Markl G (2009). Hydrothermal vein formation by extension-driven
1065   dewatering of the middle crust: an example from SW Germany. Earth and Planetary
1066   Science Letters 286:387-395.

1067 Staude S, Göb S, Pfaff K, Ströbele F, Premo WR, Markl G (2011) Deciphering fluid sources
1068   of hydrothermal systems: a combined Sr- and S-isotope study on barite (Schwarzwald, SW
1069   Germany). Chemical Geology 286:1-20

1070 Strauss H (1997) The isotopic composition of sedimentary sulfur through time.
1071   Paleogeography, Paleoclimatology, and Paleoecology 132:97-118

1072 Subías I, Moritz R, Fernández-Nieto C (1998) Isotopic composition of strontium in the Valle
1073   de Tena (Spanish Central Pyrenees) fluorite deposits : relevance for the source of elements
1074   and genetic significance. Mineralium Deposita 33: 416-424

1075 Taylor RS (1982) Planetary Science: A Lunar Perspective. Houston, TX: Lunar and Planetary
1076   Institute

1077   Tisserant D (1977) Les isotopes du strontium et l'histoire hercynienne du Maroc : Etude de
1078   quelques massifs atlasiques et mésétiens. Unpublished PhD thesis, Louis Pasteur
1079   University, Strasbourg (France), p 103

1080   Torcq F, Besse J, Vaslet D, Marcoux J, Ricou LE, Halawani M, Basahel M (1997)
1081   Paleomagnetic results from Saudi Arabia and the Permo-Triassic Pangea configuration.
1082   Earth and Planetary Science Letters 148:553-567

1083   Ulrich MR, Bodnar RJ (1988) Systematics of stretching of fluid inclusions II: barite at 1 atm
1084   confining pressure. Economic Geology 83:1037-1046

1085   Valenza K, Moritz R, Mouttaqi A, Fontignie D, Sharp Z (2000) Vein and karst barite deposits
1086   in the western Jebilet of Morocco: fluid inclusion and isotope (S, O, Sr) evidence for
1087   regional fluid mixing related to Central Atlantic rifting. Economic Geology 95:587-606

1088   van Hinsberg VJ, Migdisov AA, Williams-Jones AE (2010) Reading the mineral record of
1089   fluid composition from element partitioning. Geology 38:847-850

1090   Vauchez A (1976) Les déformations anté-triasiques dans la boutonnière d'Aouli-Mibladen.
1091   CR Acad Sci Paris 282:425-428

1092   von Gehlen K (1987) Formation of Pb-Zn-F-Ba mineralization in SW Germany : a status
1093   report. Fortschritte der Mineralogie 65(1):87-113

1094   Wittig N, Pearson DG, Baker J, Duggen S, Hoernle K (2010) A major element, PGE and Re-
1095   Os isotope study of Middle Atlas (Morocco) peridotite xenoliths: evidence for coupled
1096   introduction of metasomatic sulphides and clinopyroxene. Lithos 115(1-4):15-26

1097   Wood SA (1990a) The aqueous geochemistry of the rare-earth elements and yttrium. (1).
1098   Review of available low temperature data for inorganic complexes and the inorganic REE
1099   speciation of natural waters. Chemical Geology 82:159-186

1100   Wood SA (1990b) The aqueous geochemistry of the rare-earth elements and yttrium. (2).
1101   Theoretical predictions of speciation in hydrothermal solutions to 350°C at saturation
1102   water vapor pressure. Chemical Geology 88:99-125

1103   Zhang YG, Frantz JD (1987) Determination of the homogenization temperatures and
1104   densities of supercritical fluids in the system NaCl-KCl-CaCl$_2$-H$_2$O using synthetic fluid
1105   inclusions. Chemical Geology 64:335-350

1106

1107   **Figure captions**

1108   **Figure 1.** Generalized geologic map of the Upper Moulouya District showing the regional
1109   geology, major faults, and the location of the historically mined Aouli, Mibladen and Zeida
1110   base metal ± fluorite ± barite deposits (modified after Emberger, 1965). Inset shows the

1111   location of the Upper Moulouya District within the framework of the major

1112   tectonostratigraphic domains of Morocco. The outlined boxes refer to the main fluorite-barite

1113   vein systems sampled in this study. Filled diamonds refers to sampling localities. Letters

1114   beside symbols refer to the nature of the analytical work having been done in the course of

1115   the present study (F for fluid inclusions and T for REYs).

1116

1117   **Figure 2.** Representative selected field exposures and hand specimen samples highlighting

1118   representative aspects of mineralogy, styles of open-space filling mineralization and textural

1119   variations of different ore types from the Aouli fluorite-barite ± sulphides hydrothermal vein

1120   system.

1121   A. Panoramic view, looking north, of an exploited fluorite-barite trans-tensional vein

1122   displaying sharp contact with the Liassic dolomitic host rock.

1123   B. Cm-thick, comb-textured, purple fluorite- pink crested barite vein from the main-stage

1124   (i.e., stage I) displaying fluorite and barite crystals growing symmetrically inward

1125   from the vein walls. The upside edge of the vein is marked by the development of

1126   purple fluorite followed by crested barite and ending by colloform hematite

1127   recognizable by its oxidation ochre-yellow color.

1128   C. Close up of a cm-wide Triassic arkose-hosted dissolution cavity filled with yellow

1129   cubic fluorite.

1130   D. Close up of a polished hand sample illustrating the paragenetic evolution from cubic

1131   yellow fluorite, euhedral quartz (Qz-2), and finally crested barite punctuated by fine

1132   disseminations of sulphides.

1133   **E.** Close up of a polished hand specimen of a zoned yellow fluorite exhibiting well-

1134   developed growth zones.

1135

1136   **Figure 3.** Summary of the paragenetic sequence illustrating the various hydrothermal stages

1137   depicted in the Aouli fluorite-barite ± sulphides hydrothermal vein system. Width of bars is

1138   roughly proportional to intensity or volume event.

1139

1140   **Figure 4.** Post-Archean Australian Shale (PAAS)-normalized REY patterns of various

1141   generations of fluorite from the Aouli fluorite-barite ± sulphides hydrothermal vein system,

1142   compared to the REY patterns of the associated host rocks including the Liassic dolostones,

1143   the Triassic arkoses and the Late Variscan granite. PAAS normalization values from

1144   McLennan (1989).

1145

1146 **Figure 5.** Logarithmic plot of Tb/Ca vs. Tb/La for various generations of fluorite from the
1147 Aouli fluorite-barite ± sulphides hydrothermal vein system. The pegmatitic, hydrothermal
1148 and sedimentary fields are from Möller et al. (1976).

1149

1150 **Figure 6.** Element enrichment or depletion factors for various generations of fluorite from the
1151 Aouli fluorite-barite ± sulphides hydrothermal vein system, relative to the Late Variscan
1152 Aouli granite. These factors are calculated (Gagnon et al., 2003) by dividing the average
1153 concentration of an element in the fluorite by its average concentration in granite and may
1154 represent the degree of enrichment or depletion of elements in the fluorite types relative to
1155 the granitic intrusion.

1156

1157 **Figure 7.** Frequency distribution of $\delta^{34}S$ values for various generations of barite from the
1158 Aouli fluorite-barite ± sulphides hydrothermal vein system in comparison with the sulphur
1159 isotopic range composition for global Permian-Triassic seawater sulphate (Claypool et al.,
1160 1980).

1161

1162 **Figure 8.** Sr isotopic compositions of the various generations of fluorite and barite from the
1163 the Aouli fluorite-barite ± sulphides hydrothermal vein system in comparison with the
1164 isotopic compositions of the local host rocks (i.e., Liassic dolostones, Triassic arkoses, and
1165 Late Variscan granite).

1166

1167 **Figure 9.** Geochemical plot of $^{87}Sr/^{86}Sr$ versus 1/Sr showing the isotopic compositions of the
1168 various generations of fluorite and barite from the Aouli fluorite-barite ± sulphides
1169 hydrothermal vein system compared to the compositions of the spatially associated host rocks
1170 (i.e., Liassic dolostones, Triassic arkoses, and Late Variscan granite).

1171

1172 **Figure 10.** Representative photomicrographs in plane polarized light of doubly polished thick
1173 sections showing selected petrographic relationships and types of fluid inclusions hosted in
1174 various generations of fluorite from the Aouli fluorite-barite ± sulphides hydrothermal vein
1175 system. All photomicrographs were taken at room temperature. Abbreviations: FIs = fluid
1176 inclusion; L = aqueous liquid; V = aqueous vapor; S = solid.

1177   A. Whole specimen showing clusters and trails of densely distributed liquid rich, two-phase

1178   primary and pseudosecondary fluid inclusions lining crystal growth zones of fluorite locally

1179   truncated by arrays of secondary aqueous-rich fluid inclusions.

1180   B. Close up of coexisting elongated primary inclusions type closely associated with rounded

1181   aqueous-rich fluid inclusions in fluorite.

1182   C. Detail of a liquid rich, two-phase primary fluid inclusion.

1183   D. Detail of a multi-solid fluid inclusion containing unidentified two birefringent solids.

1184

1185   **Figure 11.** Representative frequency diagrams summarizing the distribution of fluorite-

1186   hosted fluid inclusion homogenization temperatures **(A)** and related calculated salinities **(B)**

1187   from the various generations of fluorite from from the Aouli fluorite-barite hydrothermal ±

1188   sulphides vein system.

1189

1190   **Figure 12.** Homogenization temperature (T_h) vs. salinity plot of primary and

1191   pseudosecondary fluid inclusions hosted in various generations of fluorite from the Aouli

1192   fluorite-barite ± sulphides hydrothermal vein system.

1193

1194   **Figure 13.** Ternary plot of Oakes et al. (1990) showing the distribution of H_2O-$NaCl$-$CaCl_2$

1195   ratios of primary fluid inclusions hosted in various generations of fluorite from the Aouli

1196   fluorite-barite ± sulphides hydrothermal vein system.

1197

1198   **Figure 14.** Calculated PAAS-normalized REY compositions for the parent fluid (filled red

1199   triangles) which precipitated the Aouli fluorite using a lattice-strain model with parameters

1200   from van Hinsberg et al. (2010), and that corresponding to a magmatic fluid (filled dashed

1201   bleu circles) exsolved from a crystallizing granite melt using fluid-melt partition coefficients

1202   of Flynn and Burham (1978) compared to the REY patterns of the Aouli fluorite (see text for

1203   explanation). PAAS normalization values from McLennan (1989).

1204

1205   **Figure 15.** Plot showing the distribution of salinity data as a function of the fluorite-barite ±

1206   sulphides vein systems of the Aouli district. The line drawn through the data (boxes) is

1207   interpreted to represent a binary mixing line involving two fluid end-members (F_1, F_2) and is

1208   further discussed in the text.

1209

1210

1211 **Table captions**

1212 **Table 1.** LA-ICP-MS trace-element compositions (ppm) of selected variously-colored

1213 fluorite generations from the Aouli fluorite-barite ± sulphides hydrothermal vein system.

1214

1215 **Table 2.** Sulphur isotopic compositions of various generations of barite from the Aouli

1216 fluorite-barite ± sulphides hydrothermal vein system.

1217 **Table 3.** Strontium isotope compositions of variously colored and paragenetically positioned

1218 fluorite and barite separates from the Aouli fluorite-barite ± sulphides hydrothermal vein

1219 system compared to the isotopic compositions of the spatially associated host rocks (i.e.,

1220 Liassic dolostones, Triassic arkoses, and Late Variscan granite).

1221

1222 **Table 4.** Summary of microthermometric data of fluid inclusions hosted in variously-colored

1223 fluorite generations from the Aouli fluorite-barite ± sulphides hydrothermal vein system.

1224

1225

Margoum et al. Fig.1

Margoum et al. Fig. 2

Mineral \ Paragenetic stage	Main hydrothermal F-Ba ± sulfide stage "Stage I"	Late cuboctahedral stage "Stage II"	Post-ore stage "Stage III"
• **Quartz**	Qz-1 ▬ ⋯⋯⋯ Qz-2 ▬▬	Qz-3 ▬	
• **Fluorite**	Purple Green Yellow ████████	▬▬	
• **Barite**	████	▬	
• **Sulfides**	▬	▬	
• **Fe-Mn oxides- hydroxides**		▬	⋯⋯⋯⋯
• **Cerusite**			⋯⋯⋯⋯
• **Malachite**			⋯⋯⋯⋯
• **Azurite**			⋯⋯⋯⋯

Relative timing →

- - - - <5 vol %	—— >5 and <10 vol %	▬▬ >10 and <20 vol %	████ >20 and <30 vol %	████ >30 vol %
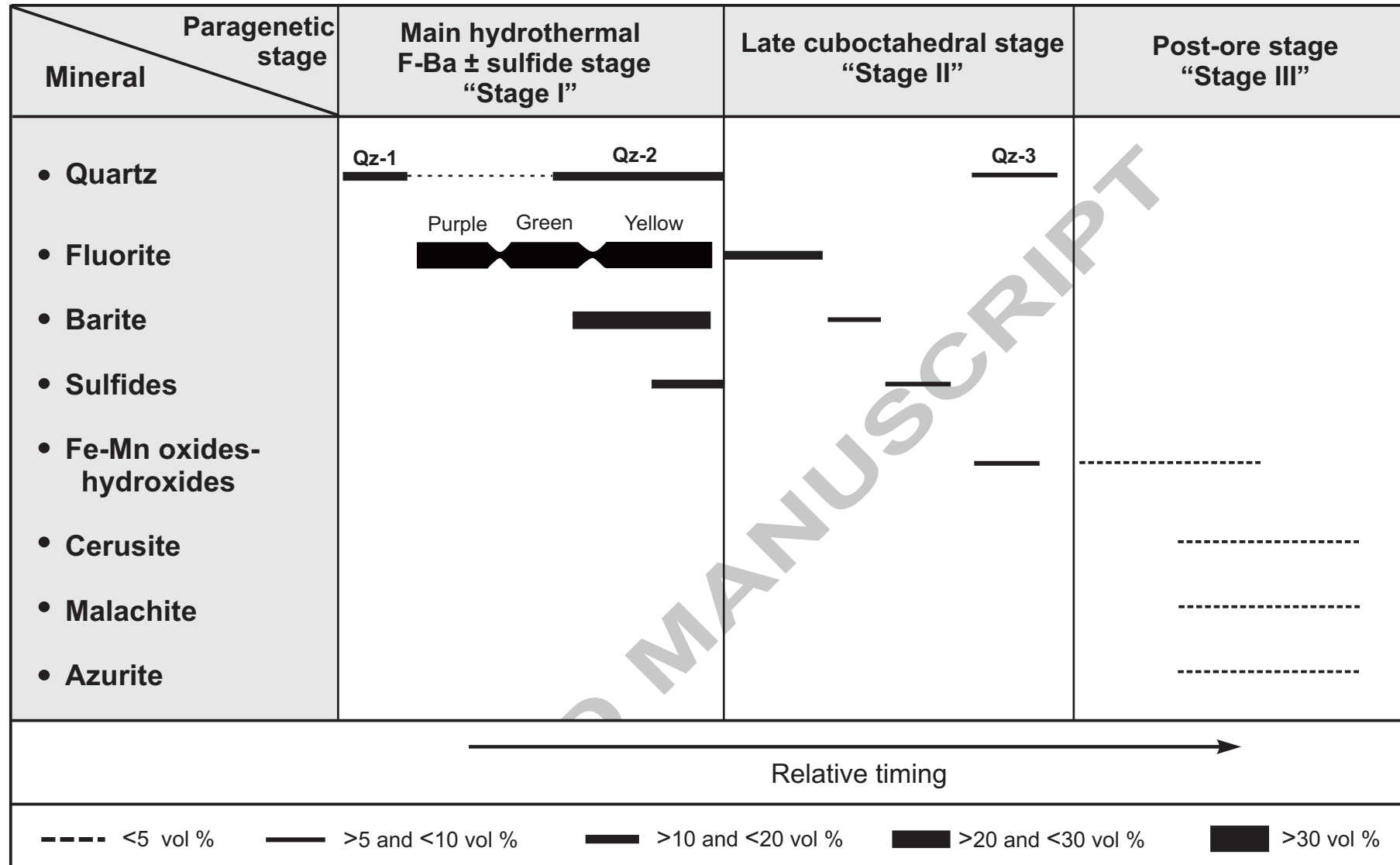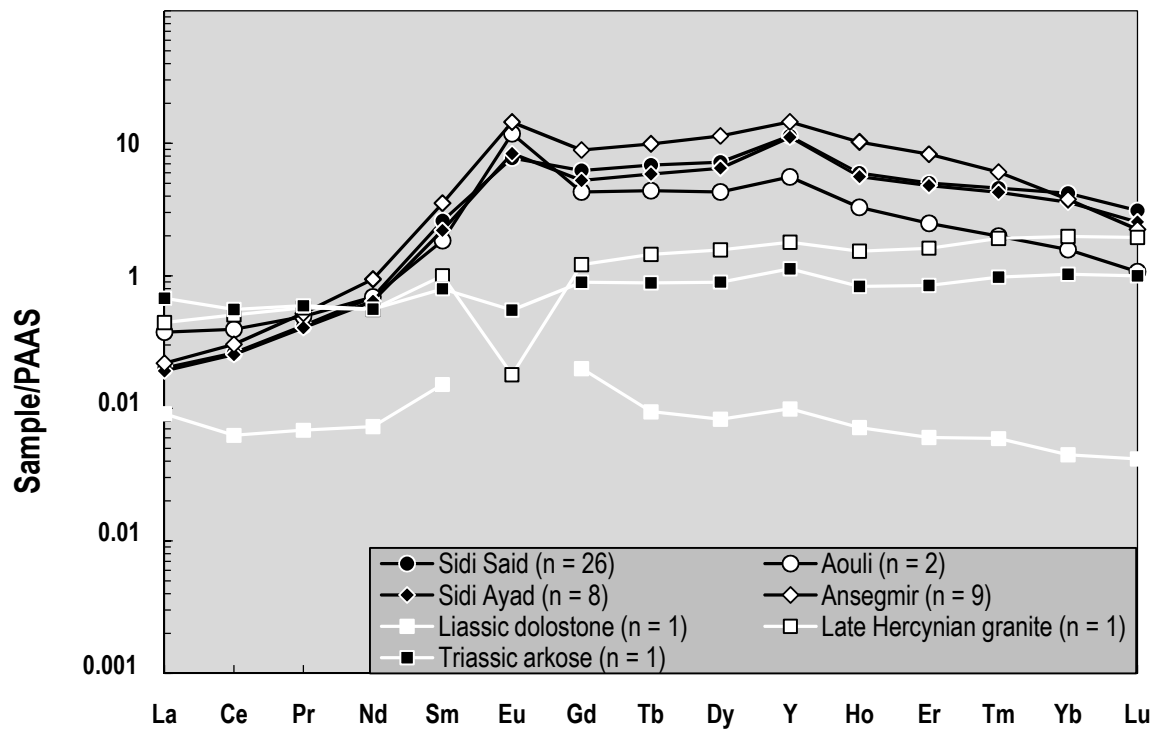
Margoum et al. Fig.3

Margoum et al. Fig. 4
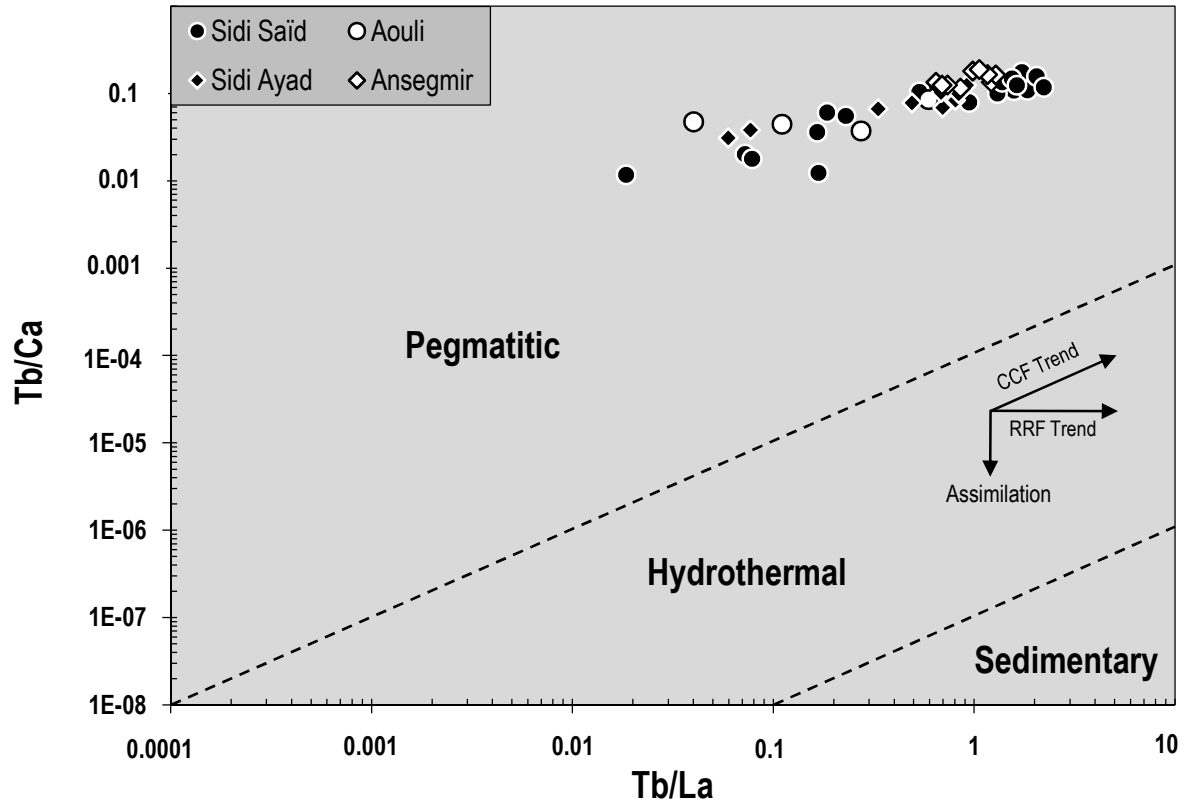
Margoum et al. Fig.5
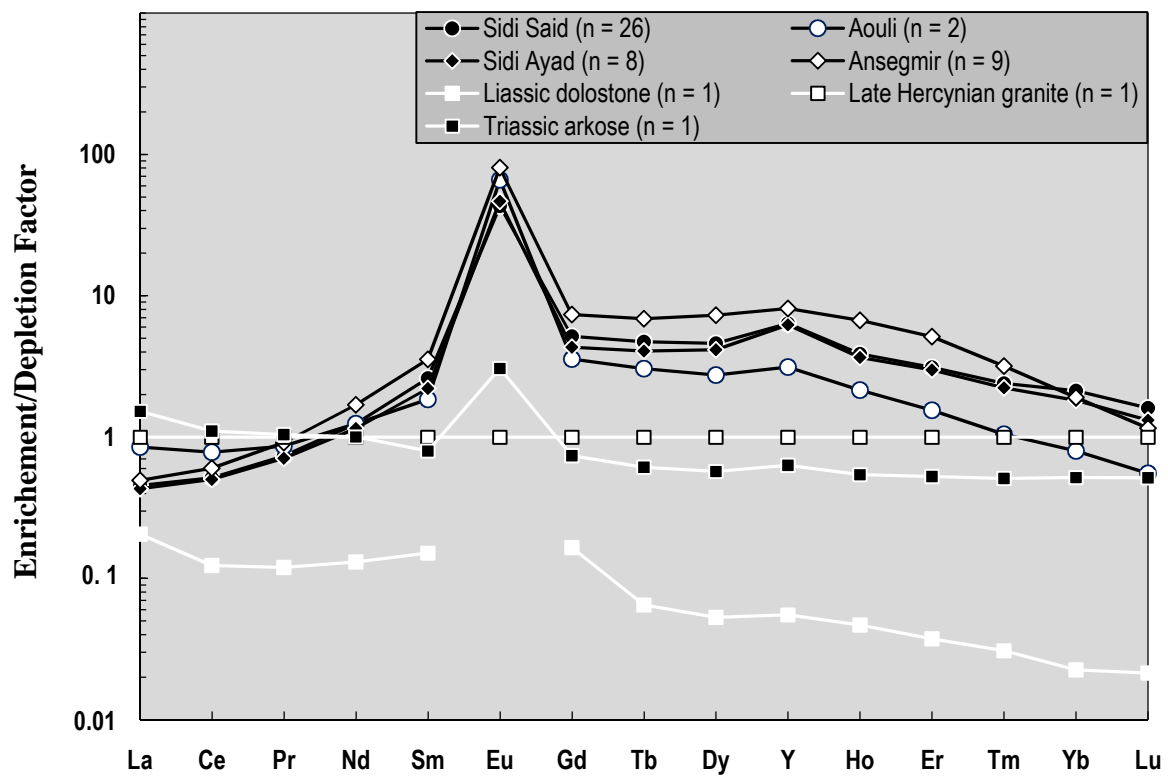
Margoum et al. Fig. 6
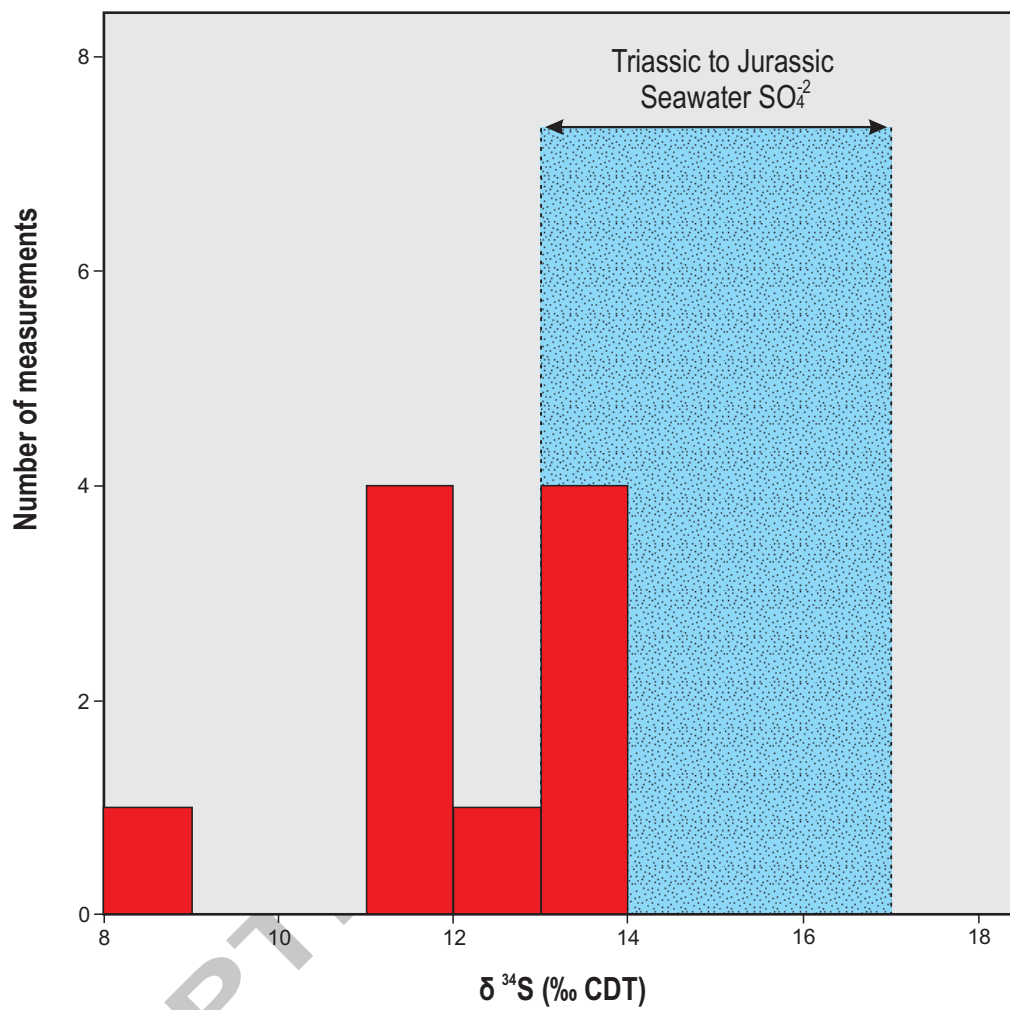
Margoum et al. Fig. 7
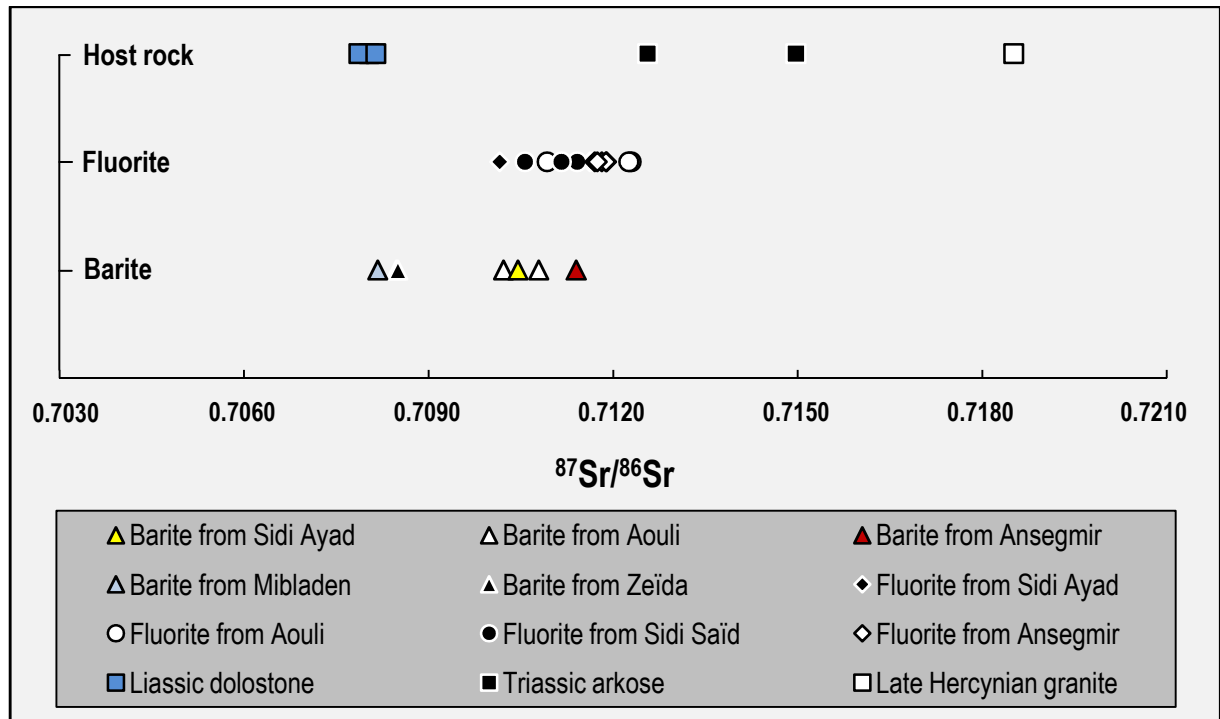
Margoum et al. Fig. 8
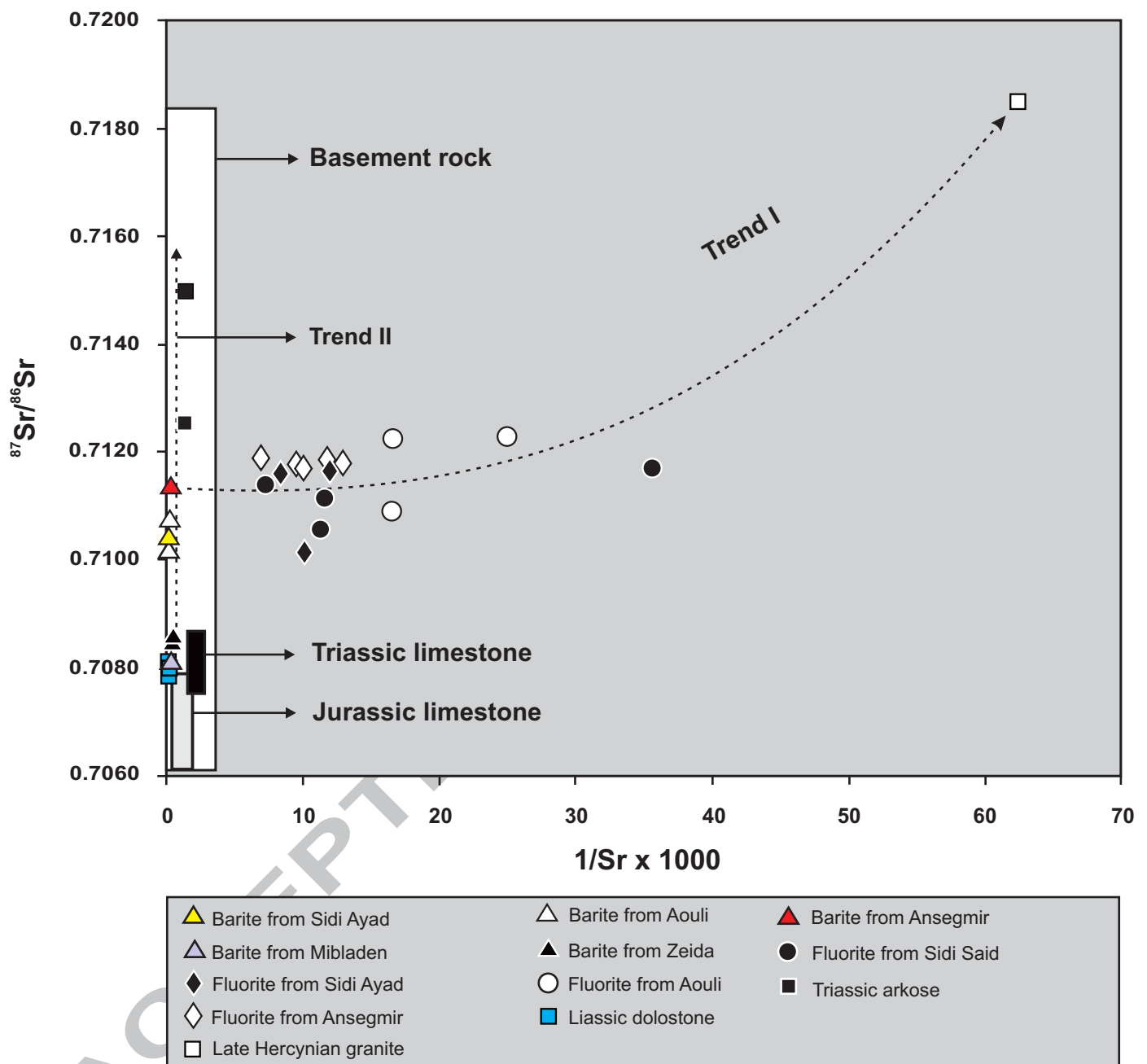
Margoum et al. Fig. 9
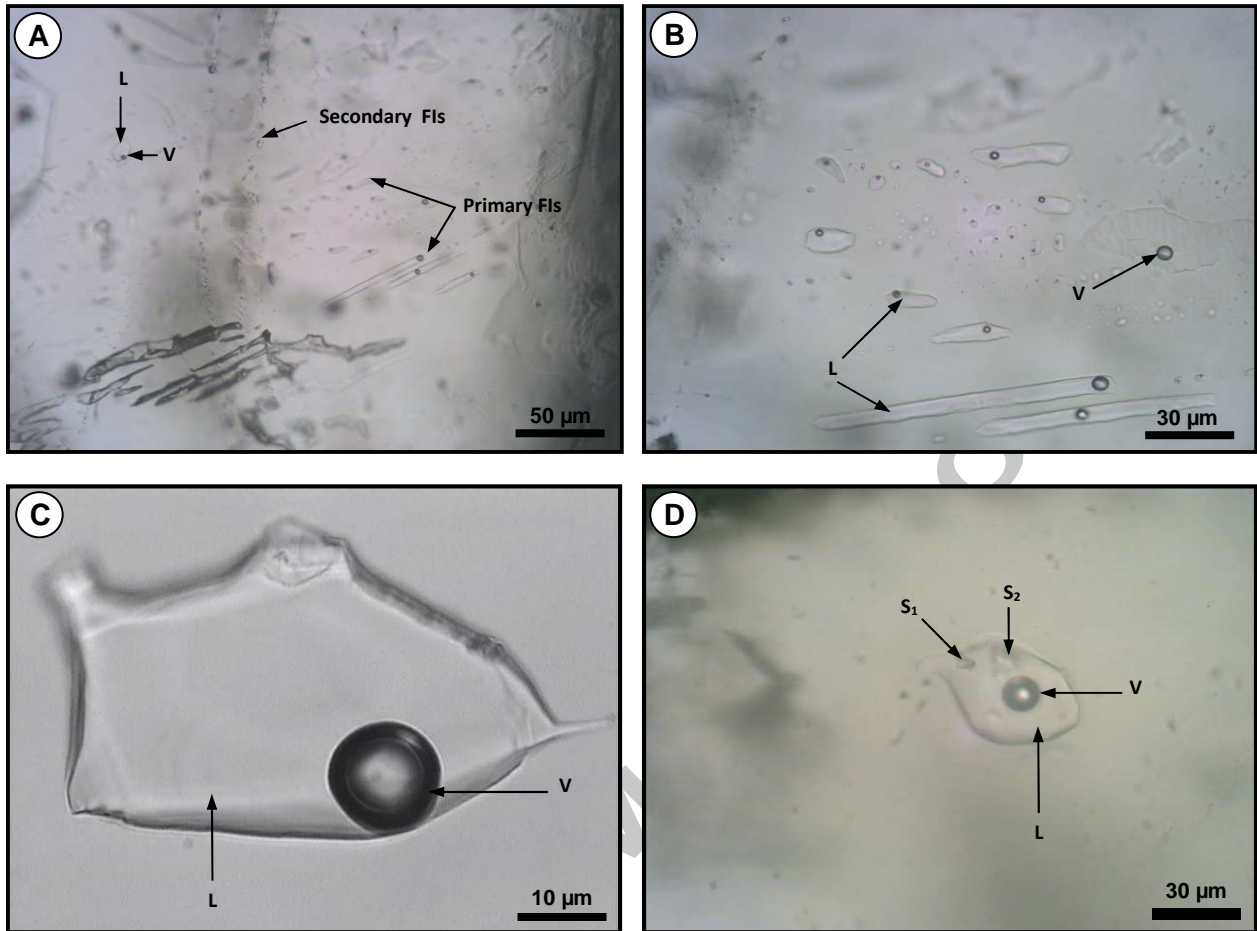
Margoum et al. Fig. 10

Margoum et al., Fig.11
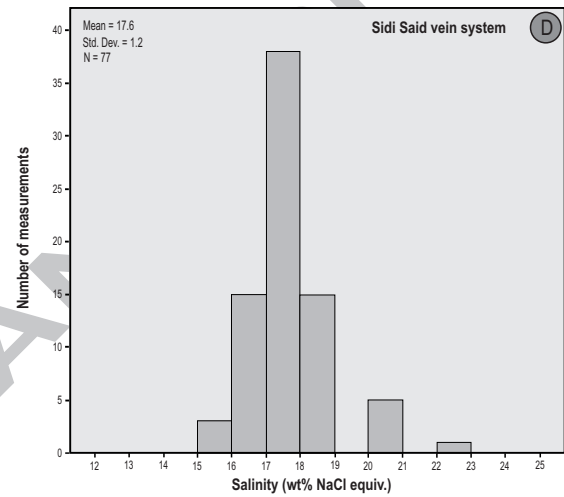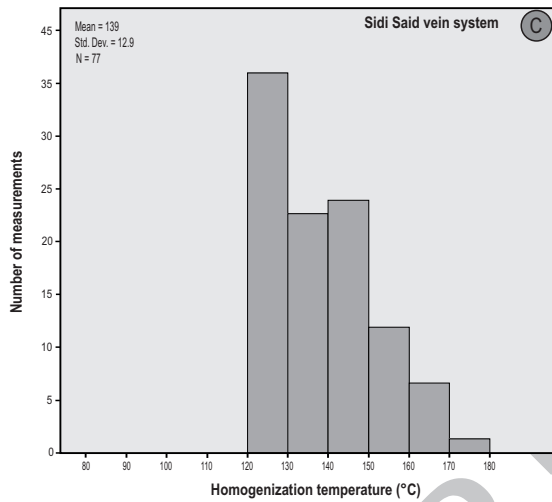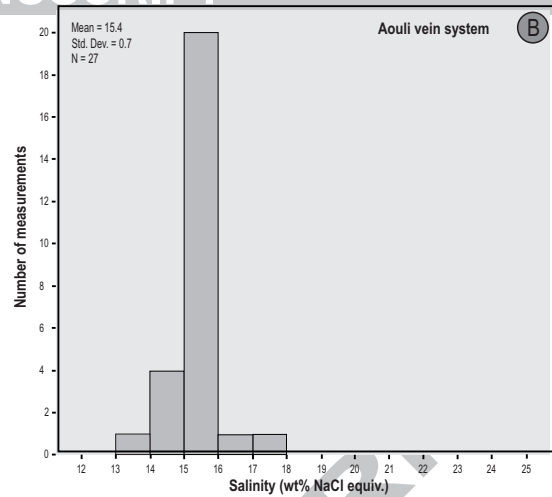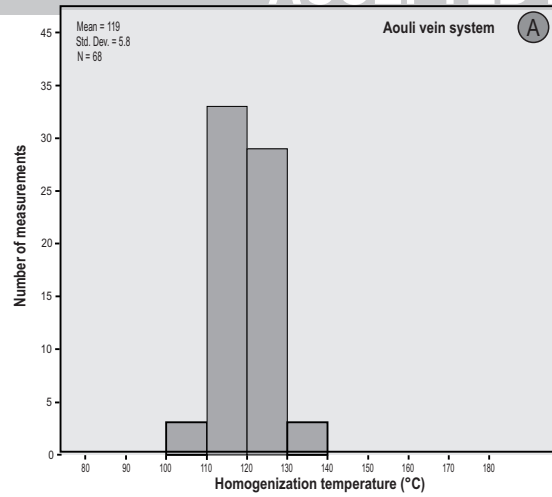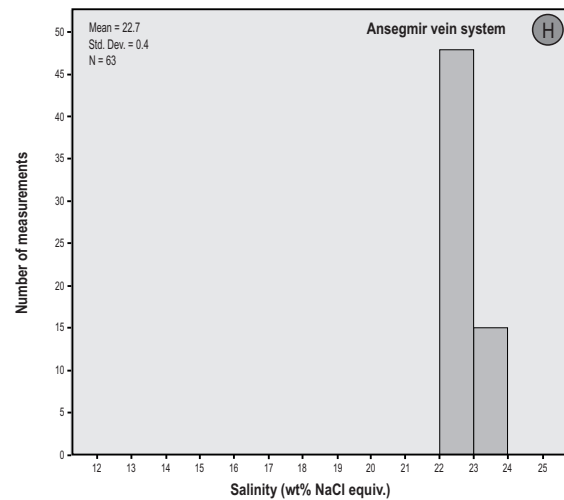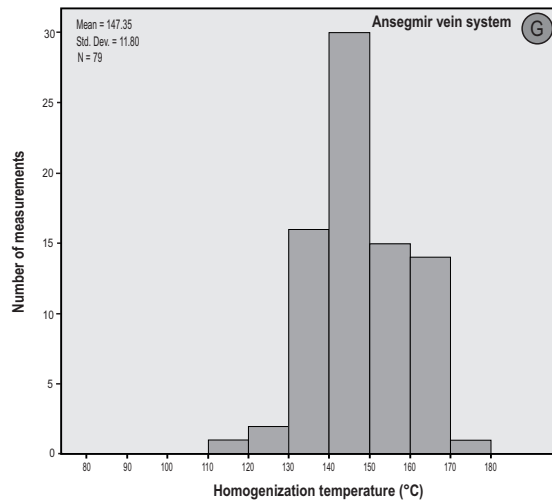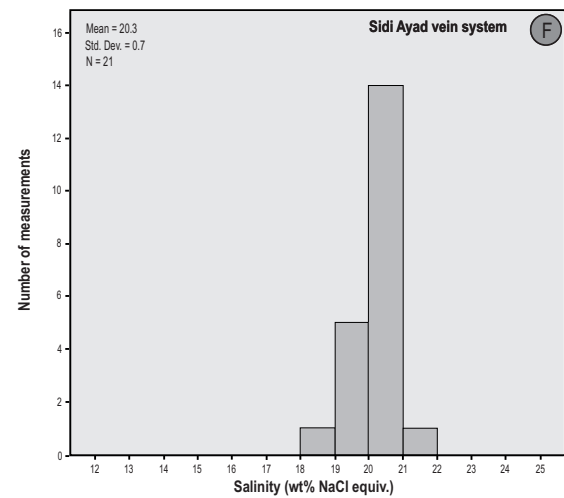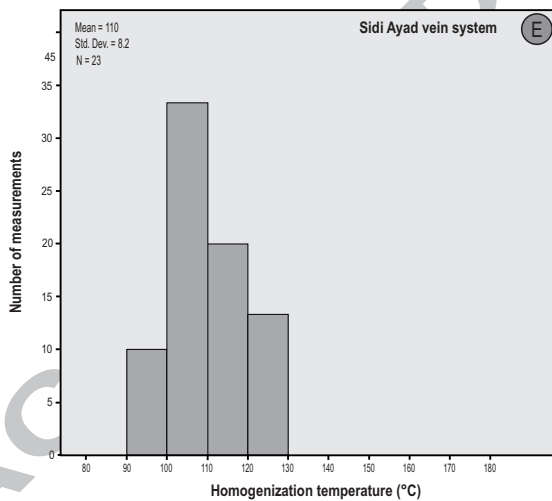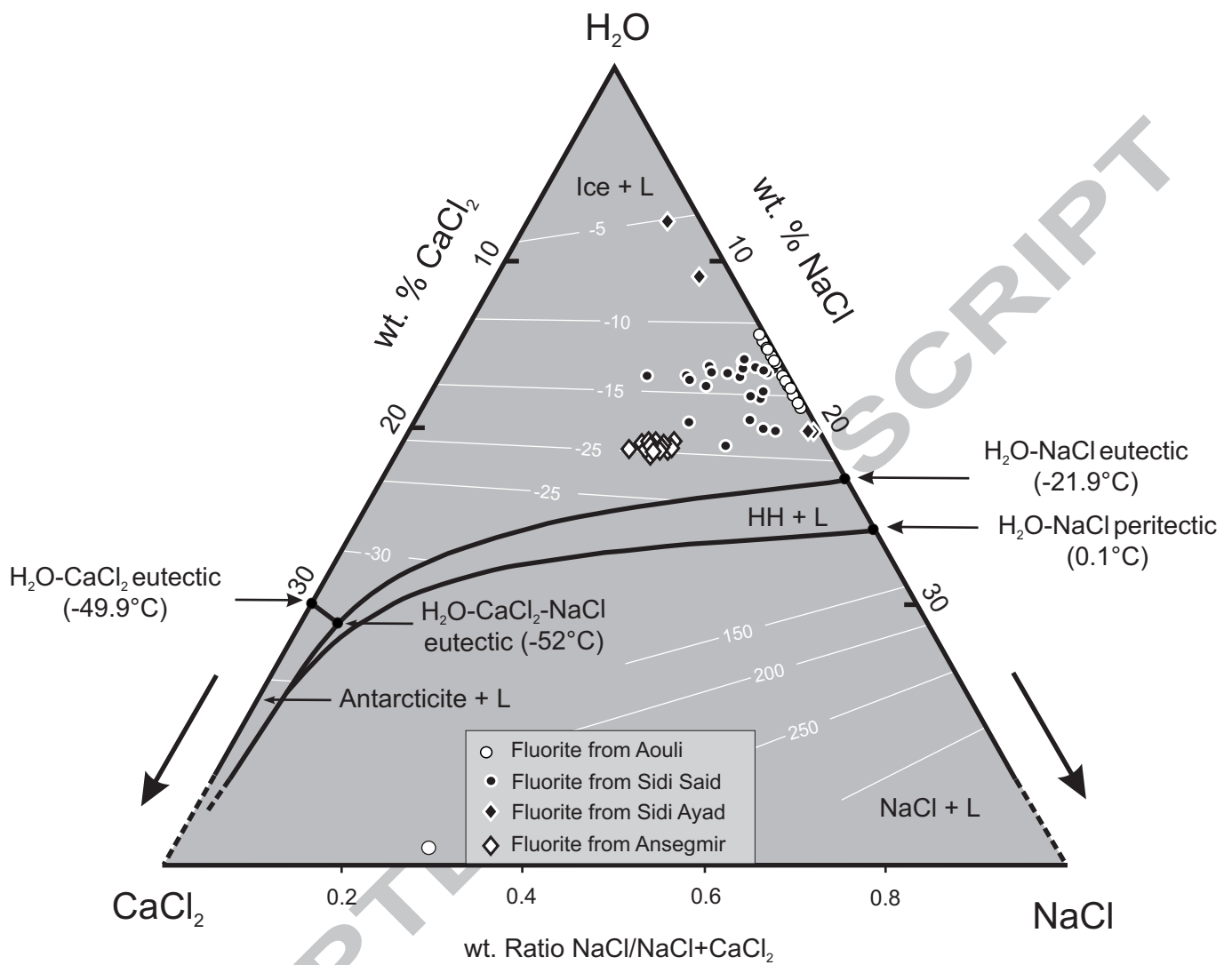
Margoum et al. Fig. 12

Margoum et al. Fig. 13
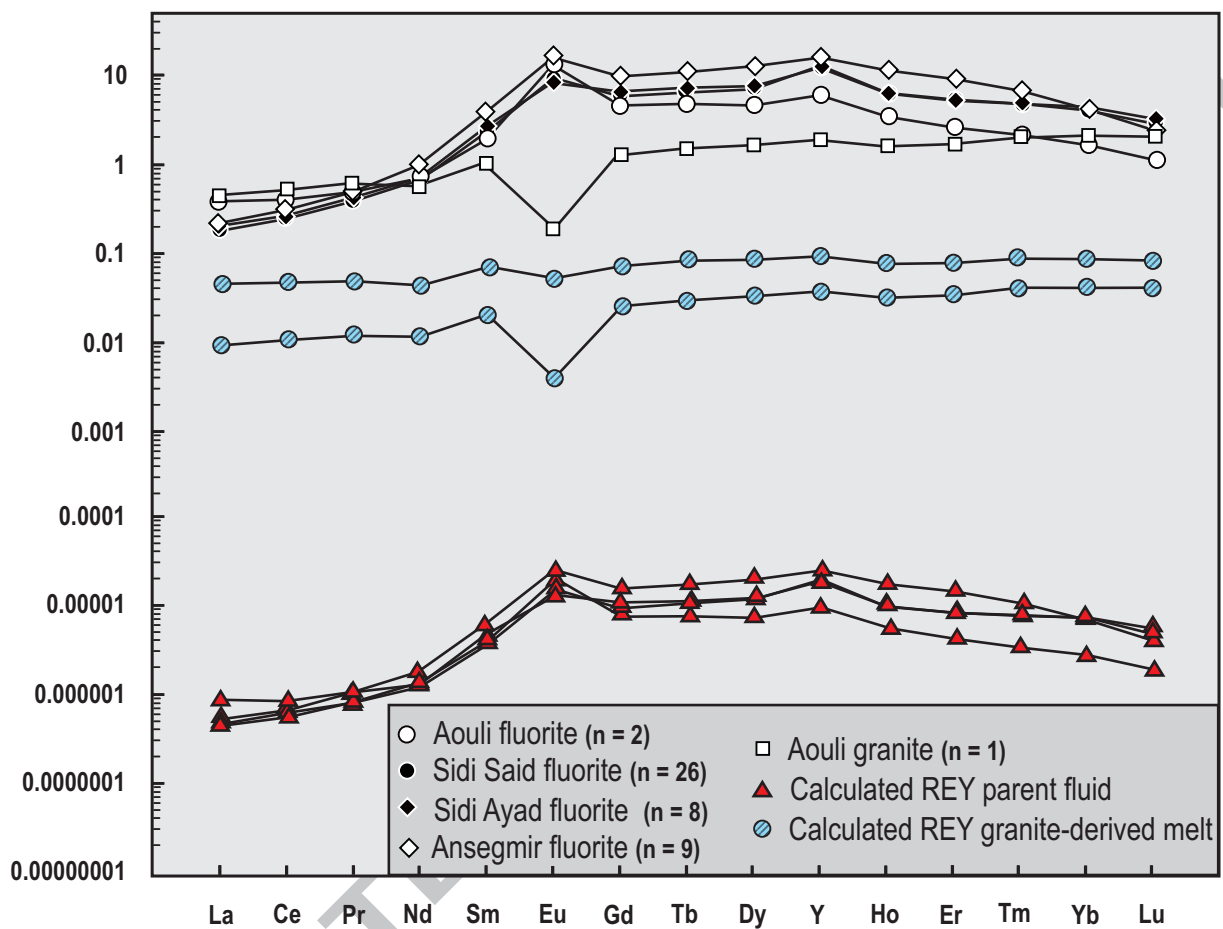
Margoum et al., Fig.14
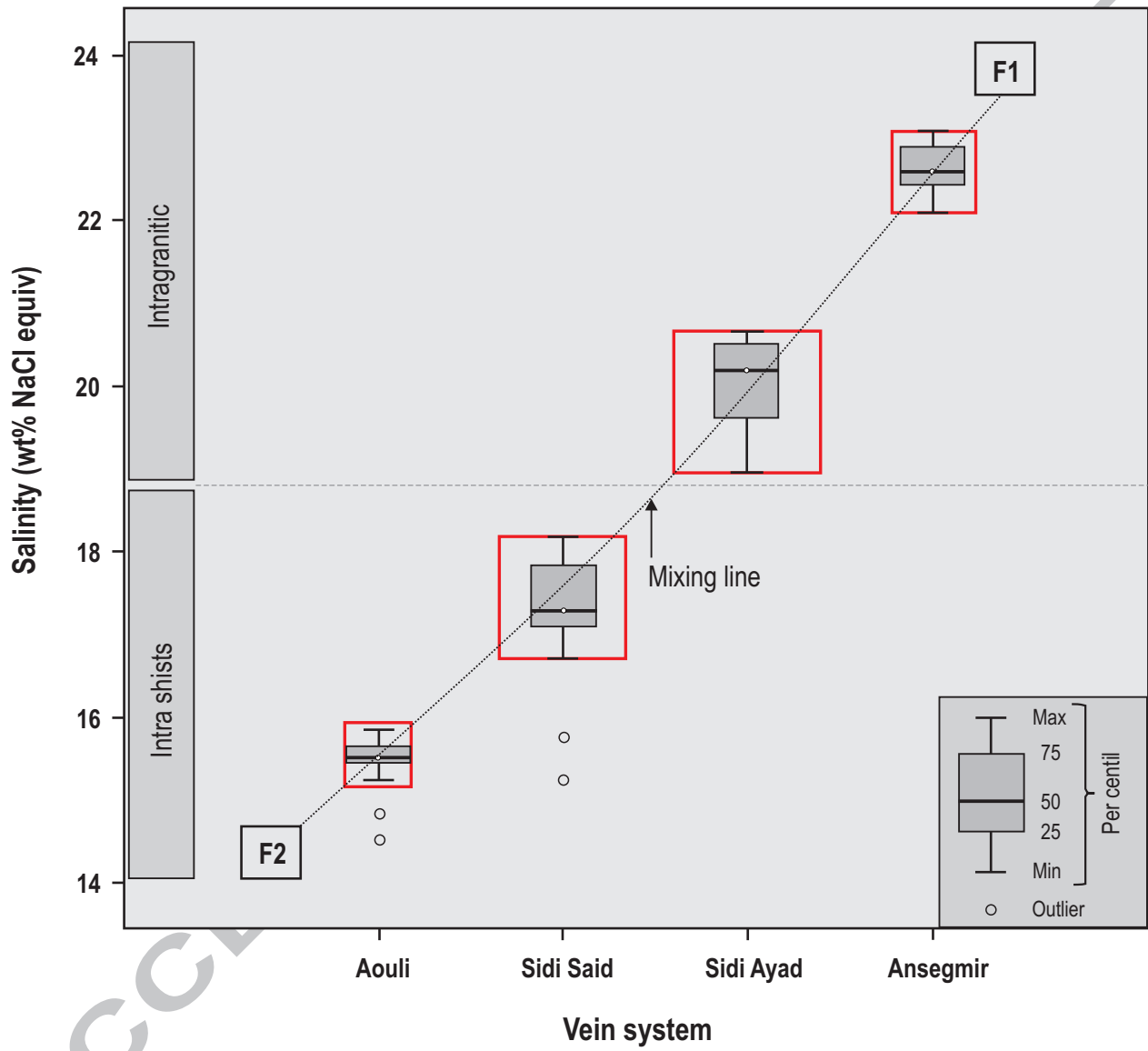
Margoum et al., Fig.15

Table 1

Mineral/Rock	Fluorite																Liassic dolostone	Late Hercynian granite	Triassic arkose
Vein system/Deposit	Sidi Ayad (n = 8)				Aouli (n = 2)				Sidi Said (n = 26)				Ansegmir (n = 9)				Mibladen (n = 1)	Aouli (n = 1)	Zeida (n = 1)
Trace elements (ppm)	Min.	Max.	Avg.	Std. Dev.	Min.	Max.	Avg.	Std. Dev.	Min.	Max.	Avg.	Std. Dev.	Min.	Max.	Avg.	Std. Dev.			
Rb	0.12	0.31	0.21	0.08	0.10	0.14	0.12	0.03	0.04	0.37	0.20	0.09	0.24	0.66	0.45	0.11	0.85	321.00	231.00
Sr	66.34	118.87	97.47	17.62	40.00	60.19	50.10	14.28	26.74	136.49	81.81	30.43	77.06	143.94	101.58	20.90	3429.00	15.94	706.70
Zr	0.011	0.03	0.02	0.01	0.01	0.03	0.018	0.01	0.003	0.13	0.02	0.02	0.01	0.025	0.02	0.01	1.81	80.93	167.90
Nb	0.00	0.018	0.00	0.01	0.00	0.00	0.00	0.00	0.00	0.01	0.00	0.00	0.00	0.01	0.00	0.00	0.22	26.29	11.40
Ba	0.35	3.76	1.10	1.15	0.88	11.55	6.21	7.55	0.22	8.57	1.14	1.54	0.54	5.47	1.68	1.48	79350.00	30.26	14860.00
La	5.20	10.55	7.14	1.77	7.56	21.22	14.39	9.65	2.80	33.41	7.83	6.47	5.85	10.95	8.40	1.68	3.48	16.94	25.85
Ce	15.18	26.41	20.00	3.74	17.83	45.24	31.53	19.38	8.08	60.73	20.94	11.90	18.22	30.79	24.39	4.55	4.98	40.39	44.46
Pr	2.88	4.32	3.54	0.51	2.91	5.83	4.37	2.07	1.27	8.50	3.72	1.55	3.48	6.03	4.66	0.97	0.60	5.06	5.26
Nd	18.50	24.85	21.74	2.57	18.45	28.52	23.49	7.12	6.83	40.40	23.44	6.95	22.70	43.73	32.41	6.78	2.47	18.92	19.04
Sm	10.90	15.61	12.46	1.59	8.53	11.97	10.25	2.43	2.46	22.30	14.26	4.51	14.03	27.18	19.96	4.09	0.84	5.54	4.43
Eu	8.36	11.05	9.15	0.91	8.99	16.59	12.79	5.38	1.84	17.98	8.27	3.48	10.89	21.07	15.98	3.72	< L.D.	0.19	0.60
Gd	18.74	33.18	25.37	4.79	14.58	25.63	20.11	7.81	4.26	49.05	28.70	11.64	31.01	56.55	42.15	7.84	0.93	5.64	4.16
Tb	3.51	6.55	4.74	1.02	2.34	4.49	3.42	1.52	0.62	9.28	5.22	2.28	6.08	9.94	7.98	1.41	0.07	1.12	0.69

Dy	24.62	43.44	31.55	6.22	13.97	26.34	20.15	8.74	3.73	59.49	33.30	14.98	41.05	68.48	54.23	11.57	0.39	7.33	4.20
Y	241.98	376.85	309.37	49.85	141.99	160.62	151.31	13.17	46.77	437.17	304.59	111.58	338.17	467.81	390.53	45.48	2.68	48.26	30.49
Ho	4.62	7.75	5.74	1.05	2.29	4.24	3.26	1.37	0.73	11.16	5.82	2.70	7.77	13.88	10.36	2.43	0.07	1.52	0.83
Er	11.47	19.47	14.21	2.86	4.80	9.42	7.11	3.27	1.78	27.65	14.17	6.75	17.17	32.33	24.07	6.07	0.17	4.40	2.41
Tm	1.38	2.58	1.81	0.44	0.52	1.10	0.81	0.41	0.19	3.74	1.84	0.91	1.67	3.69	2.52	0.78	0.02	0.78	0.40
Yb	7.09	15.82	10.73	3.14	2.53	6.38	4.46	2.72	1.14	23.14	11.74	5.93	6.58	16.39	10.92	3.76	0.13	5.58	2.89
Lu	0.70	1.77	1.18	0.39	0.26	0.67	0.47	0.29	0.11	2.65	1.34	0.69	0.59	1.47	0.10	0.36	0.02	0.84	0.43
∑REY	378.66	567.48	478.73	69.76	295.57	320.25	307.91	17.45	84.13	709.75	485.14	153.74	553.24	719.02	649.36	60.06	16.86	162.72	146.12
Hf	0.00	0.01	0.01	0.00	0.01	0.01	0.01	0.00	0.00	0.04	0.01	0.01	0.00	0.02	0.01	0.01	0.05	3.43	4.54
Ta	0.00	0.00	0.00	0.00	0.00	0.00	0.00	0.00	0.00	0.00	0.00	0.00	0.00	0.00	0.00	0.00	0.02	4.70	1.65
Th	0.00	0.04	0.02	0.01	0.08	0.35	0.21	0.19	0.00	0.15	0.02	0.04	0.00	0.04	0.02	0.02	0.07	31.11	12.59
U	0.00	0.02	0.01	0.01	0.00	0.00	0.00	0.00	0.00	0.12	0.01	0.02	0.00	0.00	0.00	0.00	0.43	4.09	4.51
Tb/La	0.33	0.92	0.70	0.20	0.11	0.59	0.35	0.34	0.02	2.22	1.05	0.69	0.65	1.28	0.96	0.24	0.02	0.07	0.03
Tb/Ca	0.07	0.12	0.09	0.02	0.05	0.09	0.07	0.03	0.01	0.18	0.10	0.04	0.12	0.19	0.15	0.03	---	---	---
Y/Ho	42.35	58.83	54.31	5.63	33.53	70.05	51.79	25.82	34.93	186.25	59.62	27.48	25.07	54.87	39.61	10.36	37.69	31.75	36.91
Sm/Yb	0.99	1.70	1.21	0.25	1.88	3.37	2.62	1.06	0.90	3.51	1.51	0.72	1.20	3.08	1.98	0.64	6.68	0.99	1.53
(La/Lu)PAAS	0.08	0.07	0.07	0.05	0.33	0.36	0.35	0.38	0.28	0.14	0.07	0.10	0.11	0.08	0.10	0.05	2.19	0.23	0.68
(Eu/Eu*)PAAS	2.25	2.76	2.45	0.20	3.79	4.46	4.13	0.47	1.42	3.50	1.95	0.50	2.36	2.98	2.58	0.20	---	0.16	0.65

Abbreviations: Min = minimum; Max = maximum; Avg. = average; Std. Dev. = Standard Deviation; L.D. = Limit Detection.

1229

Table 2

Sample No.	Vein system/Deposit	Petrographic description	$\delta^{34}S$ (‰ CDT)
11-ALB$_1$	Aouli	Vug filling white to pink crested barite associaited with quartz and sulfides	13.0
11-ALB$_2$	Aouli	Vein filling weakly silicified white barite	13.4
11-ALB$_3$	Aouli	Veinlet filling white barite cross-cutting Cambro-Ordovician schsit	8.6
11-ALB$_4$	Aouli	Translucent to white crested barite growing up on cubic fluorite	12.3
11-ALB$_5$	Aouli	Crested white barite encrusted by quartz and sulfides	13.2
11-ALB$_6$	Aouli	Crested white barite growing up on euhedral quartz	13.3
11-SDB1	Sidi Ayad	Cresetd white barite associated with fluorite	11.5
11-ASB$_1$	Ansegmir	Crested pink barite encrusted by quartz and sulfides	11.1
11-ZDB$_1$	Zeida	Vug filling white to pink barite within Triassic arkose	11.2
11-ZDB$_2$	Zeida	Vug filling white to pink barite within Triassic arkose	11.0

1230

1231

1232

1233

Table 3

Samples No.	Vein system/Deposit	Analyzed mineral/Rock	Description	Present day $^{87}Sr/^{86}Sr \pm 2\sigma$	Rb (ppm)	Sr (ppm)	$(^{87}Sr/^{86}Sr)_{250} \pm 2\sigma$
Mineral separates							
11-ALF$_1$	**Aouli**	**Fluorite**	Massive green-colored fluorite	0.712293±13		40	
11-ALF$_2$	**Aouli**	**Fluorite**	Massive green-colored fluorite	0.712254±6		60	
11-ALF$_3$	**Aouli**	**Fluorite**	Yellow cubic fluorite lining vug	0.710923±16		60	
11-SDF$_1$	**Sidi Ayad**	**Fluorite**	Crystalline translucent yellow fluorite associated with crested barite	0.710155±6		99	
11-SDF$_2$	**Sidi Ayad**	**Fluorite**	Green cubic fluorite crystal lining vug	0.711621±14		119	
11-SDF$_3$	**Sidi Ayad**	**Fluorite**	Crystalline translucent yellow fluorite	0.711671±31		83	
11-SDF$_3$	**Sidi Ayad**	**Fluorite**	Crystalline translucent yellow fluorite	0.710453±8		75	
11-SSF$_1$	**Sidi Saïd**	**Fluorite**	Crystalline yellow fluorite associated with crested barite	0.711706±14		28	
11-SSF$_2$	**Sidi Saïd**	**Fluorite**	Translucent cubic fluorite crystal lining vug	0.711415±15		136	
11-SSF$_3$	**Sidi Saïd**	**Fluorite**	Yellow honey cubic fluorite lining vug	0.711160±9		86	
11-SSF$_4$	**Sidi Saïd**	**Fluorite**	Yellow honey cubic fluorite lining vug	0.710566±11		89	
11-ASF$_1$	**Ansegmir**	**Fluorite**	Yellow honey cubic fluorite lining vug	0.711893±13		85	
11-ASF$_2$	**Ansegmir**	**Fluorite**	Crystalline yellow fluorite associated with crested barite	0.711817±14		77	
11-ASF$_3$	**Ansegmir**	**Fluorite**	Yellow honey cubic fluorite lining vug	0.711881±6		144	
11-ASF$_4$	**Ansegmir**	**Fluorite**	Cm-sized, rounded clast of purple fluorite associatade with barite and quartz	0.711701±9		100	
11-ASF$_5$	**Ansegmir**	**Fluorite**	Crystalline translucent yellow fluorite	0.711741±12		104	

Sample	Location	Type	Description	$^{87}Sr/^{86}Sr$	Rb/Sr	Sr	$(^{87}Sr/^{86}Sr)_i$
11-MBB₁	**Mibladen**	**Barite**	Crested pink barite encrusted on galena	0.708173±5		3125	
11-ZDB₁	**Zeida**	**Barite**	Vug filling crested pink barite within Triassic arkose	0.708473±8		1945	
11-ZDB₂	**Zeida**	**Barite**	Vug filling crested pink barite within Triassic arkose	0.708500±6		2354	
11-ASB₁	**Ansegmir**	**Barite**	Crested pink barite encrusted on galena and associated quartz	0.711401±5		2761	
11-ALB₁	**Aouli**	**Barite**	Bladded weakly silicified white massive barite	0.710789±9		4255	
11-ALB₂	**Aouli**	**Barite**	Crystalline translucent barite	0.710215±6		5143	
Whole rock							
11-MBD₁	**Mibladen**	**Liassic dolostone**	Early Jurassic weakly silicified medium-grained gray dolomitized dolostone	0.708030±15	0.9	3429	0.708028±15
11-MBD₂	**Mibladen**	**Liassic dolostone**	Early Jurassic weakly silicified medium-grained gray dolomitized dolostone	0.707867±13	0.7	3125	0.707865±13
11-MBD₃	**Mibladen**	**Liassic dolostone**	Early Jurassic weakly silicified medium-grained gray dolomitized dolostone	0.708140±12	0.9	3450	0.708137±12
11-ZDA₁	**Zeida**	**Traissic arkose**	Conglometric polygenic Triassic arkose	0.714997±4	231	707	0.712341±4
11-ZDA₂	**Zeida**	**Traissic arkose**	Conglometric polygenic Triassic arkose	0.712558±17	235	710	0.709867±17
11-ALG₁	**Aouli**	**Late Hercynian granite**	Muscovite-bearing leucogranite	0.718510±21	321	16	Open system

1234

1235

1236

1237

Table 4

Vein System	T_e				$T_{m(ice)}$					$T_{m(hh)}$					T_h					Salinity				
	n	Min	Max	Avg.	n	Min	Max	Avg.	Std. Dev	n	Min	Max	Avg.	Std. Dev	n	Min	Max	Avg.	Std. Dev	n	Min	Max	Avg.	Std. Dev
Aouli	64	-85	-44	-61	27	-13	-10	-11.4	0.6	21	-20.9	-19.6	-20.3	0.4	68	101	140	120	6	27	14.3	16.9	15.4	0.6
Sidi Ayad	23	-90	-50	-61	21	-18.8	-15.2	-13.8	0.8	15	-21.3	-19	-16.9	0.7	23	94	124	114	8	21	18.8	21.5	19.1	0.6
Sidi Said	81	-80	-45	-60	77	-19.1	-11.2	-13.7	1.4	41	-24.8	-20.9	-20.6	6.8	77	122	175	139	13	77	15.2	21.8	17.5	1.2
Ansegmir	62	-93	-60	-76	63	-21.6	-19.2	-20.1	0.5	26	-25.5	-24.2	-24.8	0.3	79	118	170	147	12	63	21.8	23.4	22.5	0.4

Abbreviation: Avg. = Average; n = Number of measurements; Max = Maximum; Min = Minimum; Std. Dev = Standard Deviation

1238

1239

Highlights

1. We performed REE, fluid inclusions and Sr and S isotope analysis.

2. fluorite mineralization is related to Pangean rifting and pre- Atlantic opening.

3. Ore-fluids were hot saline sedimentary brines from 2 distinct sources.

4. Water-rock interactions released REE and metals to the ore fluids largely from the granites.

5. Mixing and cooling were the main causes of ore deposition.